

# Experimental realization of a photonic weighted graph state for quantum metrology

Unathi Skosana,<sup>1,\*</sup> Byron Alexander,<sup>1</sup> Changhyoup Lee,<sup>2</sup> and Mark Tame<sup>1</sup>

<sup>1</sup>*Department of Physics, Stellenbosch University, Matieland 7602, South Africa*

<sup>2</sup>*Department of Physics, Hanyang University, Seoul 04763, South Korea*

Quantum metrology seeks to push the boundaries of measurement precision by harnessing quantum phenomena. Conventional methods often rely on maximally entangled resources, with states that are usually challenging to produce and sustain in practical setups. Here, we show that the maximally entangled constraint can be lifted by experimentally realizing a photonic two-qubit weighted graph state with an arbitrarily tunable graph weight. We use the generated state as a resource for quantum-enhanced phase sensing. We experimentally characterize the state and study its minimum estimator variance for two distinct local measurement bases as the graph weight varies from the maximally entangled to weakly entangled limit. We find excellent quantitative agreement with theoretical predictions, and observe a gain in precision beyond the classically attainable precision limit for graph weights substantially below the maximally entangled limit. This confirms that considerably less entanglement is required to achieve a quantum advantage. Albeit non-scalable in our test setup, this work represents the first experimental realization of weighted graph states with a tunable graph weight using linear optics. We expect more scalable versions of the model to be possible in an on-chip photonic platform.

## I. INTRODUCTION

Graph states [1, 2] are highly entangled quantum states that serve as essential primitives for a wide range of quantum information applications. Initially conceived as a canonical resource for measurement-based universal quantum computation [3–5], graph states have since become crucial for many other applications. These include being used as moderately sized resource states in fusion-based universal quantum computation [6, 7], quantum communication protocols such as entanglement purification [8], secret sharing [9], and quantum-enhanced metrology [10, 11]. A major drawback is that the realization of graph states is experimentally challenging. Among the physical architectures on which graph states have been realized, which include superconducting circuits [12, 13], individually addressable single-atoms [7, 14], trapped ions [15–19], neutral atoms [20], nitrogen-vacancy centers [21], and quantum dots [22–24], photonic architectures offer many advantages for quantum information: they are operational at room temperature, possess long coherence times, and provide a natural substrate for quantum communication [25–27].

The generation of photon-photon entanglement for creating quantum resources such as graph states and carrying out quantum information processing utilizes several key approaches. These include probabilistic photon-photon entanglement generation schemes that use only linear optical elements [28–30], and those that additionally rely on single-photon sources based on spontaneous parametric down-conversion (SPDC) [4, 31–34] to achieve higher success rates than the former schemes, and very-large-scale-integration technologies that combine both schemes to achieve miniaturization, modularity and scalability [35–38]. Alternatively, light-matter interaction techniques, such as those leveraging highly coupled cavity-QED systems and emitter-based schemes, can enable deterministic entanglement generation [39–45].

The generation procedure of graph states in particular requires the faithful realization of pairwise maximally entangling controlled-Z (CZ) gates to yield high-fidelity states. The controlled-Z gate is rarely experimentally realized with unit gate fidelity, and often results in a pairwise entangling gate that implements a controlled-phase gate with arbitrary phase in photonic [39–44, 46] and other physical systems [47, 48]. When the controlled-Z gates in the generation procedure of graph states are replaced by controlled-phase gates, with the value of phases representing weights of the edges between vertices, the resulting quantum states are called weighted graph states [49–51]. Such quantum states can be seen as a generalization of standard graph states, where the  $\pi$  phase due to the controlled-Z gates between the graph vertices is replaced by an arbitrary phase value  $\phi$  due to controlled-phase gates.

Weighted graph states inherit many of the properties of standard graph states, while their generality broadens their utility across quantum information science. A few select examples include the use of weighted graph states from a computational standpoint as a variational ansatz for approximating the ground state of strongly interacting spin systems such as Ising models [52, 53]. Furthermore, weighted graph states can be leveraged in measurement-based quantum computation for generating random quantum circuits [54] and the realization of a measurement-based Toffoli gate [55], efficient polynomial-time fidelity estimation protocols [56], and the detection of transitions in variable-range interaction spin models [57]. In fusion-based quantum computation, the use of weighted graph states can lead to a higher success probability for the fusion process [58]. Weighted graph states have also been proposed as a direct resource for use in quantum metrological applications such as quantum sensing [59, 60]. This is in contrast to treating weighted graph states as an intermediary and imperfect resource state to produce standard graph states, as done in entanglement concentration protocols [61–70].

---

\* [ukskosana@gmail.com](mailto:ukskosana@gmail.com)

The inherent tunability of weighted graph states via the tunable graph weights can be leveraged to achieve high-precision measurement of a physical parameter beyond classical limits. When utilizing sub-classes of weighted graph states for quantum sensing it is possible to maintain a quantum advantage for non-maximal graph weights [60]. This enables the systematic balancing of a trade-off between entanglement and precision under practical constraints, either due to imperfect or restricted experimental apparatus. The trade-off allows one to identify regimes where reduced entanglement is sufficient for an enhanced metrological performance, this represents a distinct advantage over standard graph states with a fixed topology and graph weights. Despite the compelling evidence from the theoretical framework establishing the robustness of weighted graph states for metrological applications in Ref. [60] and the complementary strengths of photonic architectures, to date no experimental work exists utilizing photonic weighted graph states as a direct resource for quantum metrology.

In this study, we demonstrate the experimental realization of a photonic two-qubit weighted graph state with a tunable graph weight using linear optics and a single polarization-entangled photon-pair source based on SPDC. We use the photonic weighted graph state for the metrological task of sensing a parameter  $\theta$  associated with a unitary transformation  $U(\theta)$  to the highest precision possible. Here, we vary the graph weight between  $\pi$  (standard two-qubit graph state) and 0 (product state), and show sensing precision beyond the classical limit for weights substantially smaller than  $\pi$ ; experimentally confirming that considerably less entanglement is sufficient for achieving a quantum advantage. This represents the first direct demonstration of a weighted graph state with a tunable weight used in a photonic quantum sensing application, bridging theory and experiment to establish photonic weighted graph states as a practical resource for quantum-enhanced metrology. Our work constitutes a proof-of-concept demonstration, and while utilizing a non-scalable optical architecture, the generation procedure presented here has the potential to be compatible with scalable platforms [39–44, 46].

The paper is organized as follows. In Sec. II we describe our experimental setup and explain implementation details. Sec. III describes the experimental results concerning state characterization. Then, in Sec. IV we describe the phase sensing protocol and experimental results. Finally, in Sec. V, we give a summary and discuss future work.

## II. EXPERIMENTAL SETUP

Our experimental scheme in Fig. 1 for generating a weighted graph state with a tunable graph weight is based on the scheme reported in Ref. [31]. The scheme consists of a polarization-entangled photon-pair source that generates the state  $|\Phi^{(-)}\rangle = (|H_1, H_2\rangle - |V_1, V_2\rangle)/\sqrt{2}$ . Here,  $H$  ( $V$ ) denotes horizontal (vertical) polarization, and the subscripts 1, 2 refer to the photons, respectively. Our photon-pair source consists of a 405 nm continuous wave diode laser (vertically polarized) as the pump beam, a half-wave plate (HWP) set to

22.5°, a quarter-wave plate (QWP) set to 10°, and two cascaded  $\beta$ -barium borate (BBO) crystals with mutually perpendicular optic axes [71]. A non-collinear type-I SPDC process in the cascaded BBO crystals generates frequency-degenerate photon pairs at a wavelength of 810 nm, emitted into a light cone with a half opening angle of 3° relative to the pump beam direction. The photon-pair source sends photon 1 to the sensing and measurement step described later. Photon 2 goes through a series of optical elements to generate the weighted graph state. First, it goes into a polarizing beam splitter (PBS), which transmits (reflects) a horizontally (vertically) polarized photon, and transforms the two-photon state  $|\Phi^{(-)}\rangle = (|H_1, H_2\rangle - |V_1, V_2\rangle)/\sqrt{2}$  to

$$|\Psi_I\rangle = (|H_1, r_2, H_2\rangle - |V_1, l_2, V_2\rangle)/\sqrt{2}, \quad (1)$$

where  $r_2$  ( $l_2$ ) refers to the transmitted (reflected) paths for photon 2, respectively, as shown in Fig. 1. Photons in both  $l_2$  and  $r_2$  go through a HWP set to 22.5° with respect to the fast axis and the vertical axis, which maps  $|H\rangle \mapsto |D\rangle$  in  $r_2$  and  $|V\rangle \mapsto |A\rangle$  in  $l_2$ , where  $|D/A\rangle = (|H\rangle \pm |V\rangle)/\sqrt{2}$ . This is followed by a configuration of QWP-HWP-QWP that implements a  $R_z(\phi'_{12})$  rotation for photons in  $l_2$  and an identity  $I$  operator in  $r_2$ , respectively. The  $R_z(\phi'_{12})$  rotation on photons in  $l_2$  is the core tuning mechanism for the graph weight. A QWP-HWP-QWP configuration can uniquely decompose a general  $SU(2)$  operator [72–74]. After these operations, the state in Eq. 1 becomes

$$|\Psi_{II}\rangle = (|H_1, r_2, D_2\rangle - e^{-i\phi'_{12}/2} |V_1, l_2, D_2^{\pi+\phi'_{12}}\rangle)/\sqrt{2}, \quad (2)$$

where  $|D^{\pi+\phi'_{12}}\rangle = (|H\rangle + e^{i(\pi+\phi'_{12})} |V\rangle)/\sqrt{2}$ . When photons from  $l_2$  and  $r_2$  combine on the input ports of the non-polarizing beam splitter (NPBS), we obtain

$$|\Psi_{III}\rangle = (e^{-i\varphi_{r_2}} (|H_1, p_2, D_2\rangle + |H_1, q_2, D_2\rangle) - e^{-i\varphi_{l_2}} e^{-i\phi'_{12}/2} (|V_1, p_2, D_2^{\pi+\phi'_{12}}\rangle - |V_1, q_2, D_2^{\pi+\phi'_{12}}\rangle))/2. \quad (3)$$

Here,  $p_2$  and  $q_2$  are the output ports of the non-polarizing beam splitter, defined by the transformations  $|r_2\rangle \rightarrow (|p_2\rangle + |q_2\rangle)/\sqrt{2}$  and  $|l_2\rangle \rightarrow (|p_2\rangle - |q_2\rangle)/\sqrt{2}$ . Moreover,  $e^{-i\varphi_{r_2}}$  and  $e^{-i\varphi_{l_2}}$  are relative phases acquired by the optical paths  $r_2$  and  $l_2$ , respectively. We take the detected photons to be from the output port  $p_2$ , giving the state

$$|\Psi_{IV}\rangle = (|H_1, D_2\rangle - e^{i\varphi'} e^{-i\phi'_{12}/2} |V_1, D_2^{\pi+\phi'_{12}}\rangle)/\sqrt{2}, \quad (4)$$

where we have collected all the  $p_2$  terms, set  $\varphi' = \varphi_{r_2} - \varphi_{l_2}$  and dropped a global phase. Denoting  $\phi_{12} = \pi + \phi'_{12}$  and  $\varphi = \varphi' - \phi'_{12}/2 + \pi$ , the expression in Eq. 4 becomes

$$|\Psi_V\rangle = (|H_1, D_2\rangle + e^{i\varphi} |V_1, D_2^{\phi_{12}}\rangle)/\sqrt{2}. \quad (5)$$

When the phase difference  $\varphi'$  between the optical path  $l_2$  and  $r_2$  becomes equal to  $\phi'_{12}/2 - \pi$  from translating the mirror

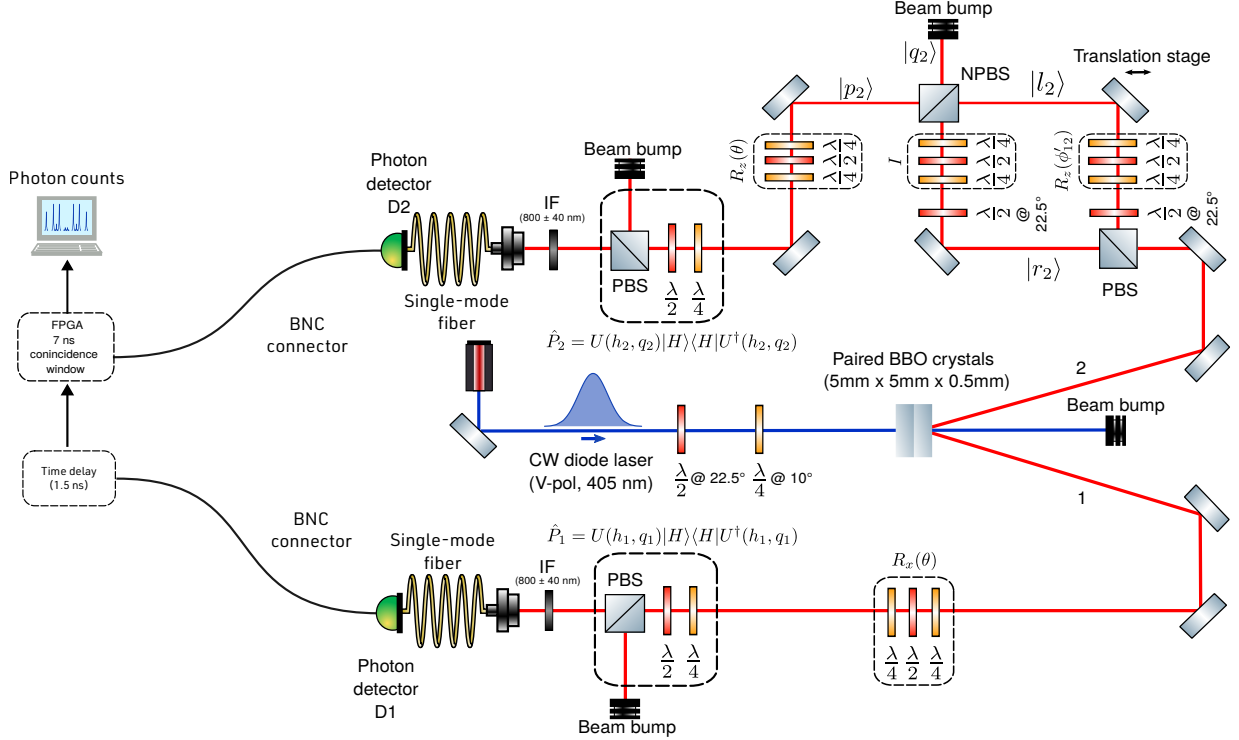


FIG. 1: Experimental setup for creating the two-qubit weighted graph  $|\Gamma_{\phi_{12}}\rangle$  with a tunable graph weight, and for performing a quantum metrology protocol. A 405 nm continuous wave (CW) diode laser pump beam (vertically polarized) passes through a half-wave plate (HWP) set to  $22.5^\circ$ , a quarter-wave plate (QWP) set to  $10^\circ$ , and two cascaded  $\beta$ -barium borate crystals (5mm by 5mm by 0.5mm each) with mutually perpendicular optic axes, to create the polarization-entangled  $|\Phi^{(-)}\rangle$  state. The generated photons are separated: photon 1 goes to a sensing stage. Photon 2 is split by a PBS into paths  $r_2$  and  $l_2$ , forming a Mach-Zehnder interferometer (MZI). The  $R_z(\phi_{12})$  rotation in path  $l_2$  (implemented by a QWP-HWP-QWP configuration) is the core tuning mechanism for the graph weight  $\phi_{12}$ . The paths recombine at a non-polarizing beam splitter (NPBS), where port  $p_2$  is selected. Both photons then enter the quantum sensing stage, where the phase  $\theta$  is encoded by the unitary  $U(\theta) = R_x^{(1)}(\theta) \otimes R_z^{(2)}(\theta)$ . Finally, both photons are detected after passing through an arbitrary polarization projective measurement (QWP-HWP-PBS), interference filters ( $800 \text{ nm} \pm 40 \text{ nm}$ ), and coupled into single-mode fibers for detection by avalanche photodiode (APD) single-photon detectors and a coincidence counting module. The detector output for photon 1 is delayed by 1.5 ns before it enters the coincidence counting module.

on the stage, then  $\varphi$  becomes equal to zero and we obtain a two-qubit weighted graph state with the graph weight  $\phi_{12}$ :

$$|\Gamma_{\phi_{12}}\rangle = (|H_1, D_2\rangle + |V_1, D_2^{\phi_{12}}\rangle)/\sqrt{2}. \quad (6)$$

In the computational basis, where  $\{|0\rangle, |1\rangle\}$  is represented by  $\{|H\rangle, |V\rangle\}$ , we have

$$|\Gamma_{\phi_{12}}\rangle = CZ^{\phi_{12}} |+\rangle_1 |+\rangle_2, \quad (7)$$

where  $CZ^{\phi_{12}} = \text{diag}(1, 1, 1, e^{i\phi_{12}})$ , giving the standard definition of a weighted graph state. To encode a phase parameter for quantum metrology, photon 1 (2) goes through a QWP-HWP-QWP configuration that implements a  $R_x(\theta)$  ( $R_z(\theta)$ ) rotation, respectively. The phase encoding unitary operator  $U(\theta) = R_x^{(1)}(\theta) \otimes R_z^{(2)}(\theta)$  is relevant in the phase sensing protocol described later. The rotation  $R_x^{(1)}(\theta)$  is equivalent to a phase rotation up to Hadamard operations, i.e.,  $R_x^{(1)}(\theta) = HR_z^{(1)}(\theta)H$ . In the initial state generation step, both sets of waveplates are configured to implement the identity operator.

The waveplate angles for each rotation and the identity operator can be found in Appendix A. The measurement steps ( $\hat{P}_1$  and  $\hat{P}_2$  in Fig. 1) for the photon pairs are identical. Each photon goes through a QWP, HWP, and PBS, where we only collect the transmitted photons. This combination of optics is capable of realizing an arbitrary polarization projective measurement. Each photon then passes through  $800 \text{ nm} \pm 40 \text{ nm}$  interference filters. Finally, the photons are coupled into single-mode fibers. The single-mode fibers are then directly coupled into silicon avalanche photodiode (APD) single-photon detectors. The detector output for photon 2 goes directly into a coincidence counting module [75] with a coincidence window of 7 ns. The detector output for photon 1 is electronically delayed by 1.5 ns before entering the coincidence counting module to compensate for the longer optical path of photon 2. This ensures both photons arrive within a single coincidence window.

### III. STATE CHARACTERIZATION

#### A. Phase stability and control

The experimental setup described in the preceding section generates the target two-qubit weighted graph state,  $|\Gamma_{\phi_{12}}\rangle$ , with a tunable graph weight  $\phi_{12}$ . Here, we characterize various aspects of the state generation. In the first instance, we characterize the control of phase difference,  $\varphi' = \varphi_{r_2} - \varphi_{l_2}$ , inside the Mach-Zehnder interferometer (MZI). This phase difference is critical for state generation; achieving the condition  $\varphi' = \varphi_{12}/2 - \pi$  is necessary to realize the desired weighted graph state. We quantify the experimental capability to distinguish between different target values of  $\varphi'$  using fringe visibility measurements. To do this, we perform fringe visibility measurements on an intermediate two-photon state,  $(|H_1, H_2\rangle - e^{i\varphi'} |V_1, H_2\rangle)/\sqrt{2}$ . In the experiment, this state is obtained from Eq. 1 by setting the HWPs inside  $l_2$  and  $r_2$  to  $45^\circ$  and  $0^\circ$ , respectively. The  $R_z(\phi'_{12})$  rotation in  $l_2$  is configured to implement the identity operator. When the polarization measurement optics project  $\hat{P}_1 \otimes \hat{P}_2 = |A_1\rangle \langle A_1| \otimes |H_2\rangle \langle H_2|$ , we obtain the following detection probability:

$$P(o_1 = A_1, o_2 = H_2) = (1 + \cos \varphi')/2. \quad (8)$$

From Eq. 8, we see that we can perform fringe visibility measurements by translating the mirror in  $l_2$  to sweep the value of  $\varphi'$  over a full cycle  $[0, 2\pi)$  and recording the coincidence photon counts. We then take the maximum and minimum coincidence counts recorded, and calculate the fringe visibility as  $V = (N_{\max} - N_{\min})/(N_{\max} + N_{\min})$ , where  $N_{\max}$  ( $N_{\min}$ ) is the maximum (minimum) photon count.

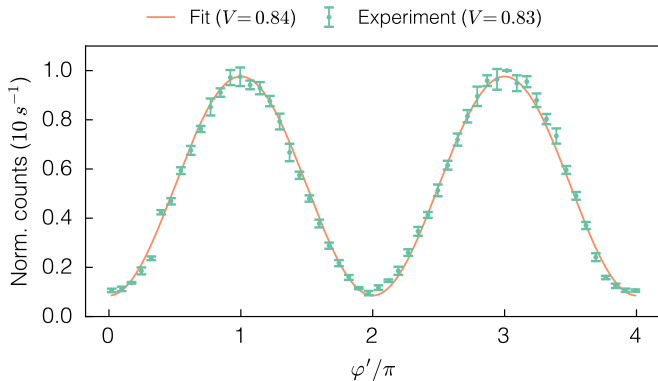


FIG. 2: Normalized photon counts and fit as a function of the phase difference between the two optical paths  $\varphi'$ , varied by translating the mirror on a stage in steps of 60 nm. Each data point is an average of 10 measurements, where each measurement is from accumulated photon counts over a 10-second interval. The normalized photon counts are fitted to  $f(x) = a \cos(bx + c) + d$ , where the parameters of the fit are  $a, b, c$  and  $d$ . The error bars represent the standard deviation of the mean. The discontinuity around the 6th step was due to a double jog. See Appendix B for more details.

Fig. 2 shows normalized photon counts as we vary  $\varphi'$ , where each data point is an average of 10 measurements, each collected over a 10-second interval, with a maximum of 150 coincidence counts per second. We achieve a fringe visibility of  $V = 83\%$ , confirming that the phase  $\varphi'$  due to the optical path length difference is stable enough to be reliably controlled. See Appendix B for more details.

#### B. Intermediate state tomography

Next, we verify the fidelity [76] of the generated state via quantum state tomography (QST). Here, the primary objective is to reconstruct the density matrix for the intermediate polarization-entangled state  $(|H_1, H_2\rangle - e^{i\varphi'} |V_1, V_2\rangle)/\sqrt{2}$  at specific targeted values for the phase  $\varphi'$ . This state is obtained by setting the HWPs inside  $l_2$  and  $r_2$  both to  $0^\circ$ . The  $R_z(\phi'_{12})$  rotation in  $l_2$  is configured to implement the identity operator. Reconstructing the two-qubit density matrix requires performing a set of 16 different, non-redundant polarization projective measurements [77]. The measurement bases are selected from the product of the three standard single-photon bases: rectilinear basis  $\{|H\rangle, |V\rangle\}$ , diagonal basis  $\{|D\rangle, |A\rangle\}$  and circular basis  $\{|R\rangle, |L\rangle\}$ . These measurements are realized experimentally by the QWP, HWP, and PBS configuration in the measurement stage, as described in the preceding section.

For each of the 16 measurement settings we record coincidence counts over a 10-second interval. The waveplate angles corresponding to each polarization measurement basis can be found in Appendix C. The experimentally determined counts are processed using a maximum likelihood estimation (MLE) algorithm that reconstructs a valid physical density matrix. In our experiment, we choose to characterize the state when  $\varphi'$  takes on the values  $\varphi' = 0, \pi/4, \pi/2, 3\pi/4, \text{ and } \pi$ . To set  $\varphi'$  to one of these values, we first monitor the photon counts for the projector  $\hat{P}_1 \otimes \hat{P}_2 = |D_1\rangle \langle D_1| \otimes |D_2\rangle \langle D_2|$ . For the intermediate state  $(|H_1, H_2\rangle - e^{i\varphi'} |V_1, V_2\rangle)/\sqrt{2}$ , this projector has the following detection probability,

$$P(o_1 = D_1, o_2 = D_2) = (1 - \cos \varphi')/2. \quad (9)$$

Thus, targeting the phases  $\varphi' = 0$  and  $\pi$  corresponds to cases where the detection probability above takes on a minimum and a maximum value, respectively. The intermediate phases are then targeted by translating the mirror inside path  $l_2$  and recording the total number of discrete steps it takes to go from the minimum to the maximum number of photon counts. Then, starting from a minimum,  $\pi/4$  corresponds to taking 25% of the total number of steps from minimum to maximum,  $\pi/2$  corresponds to 50% of the total number of steps, and so forth. While performing projective measurements, the phase  $\varphi'$  can drift from one value to another. We correct for this drift by using a ‘dither lock’ approach, where we keep track of photon counts from fixed projective measurements and use them as checkpoints in between tomography projective measurements for a particular phase. If there is a drift, we actively correct for it by translating the mirror in  $l_2$  until we recover the checkpoint value.

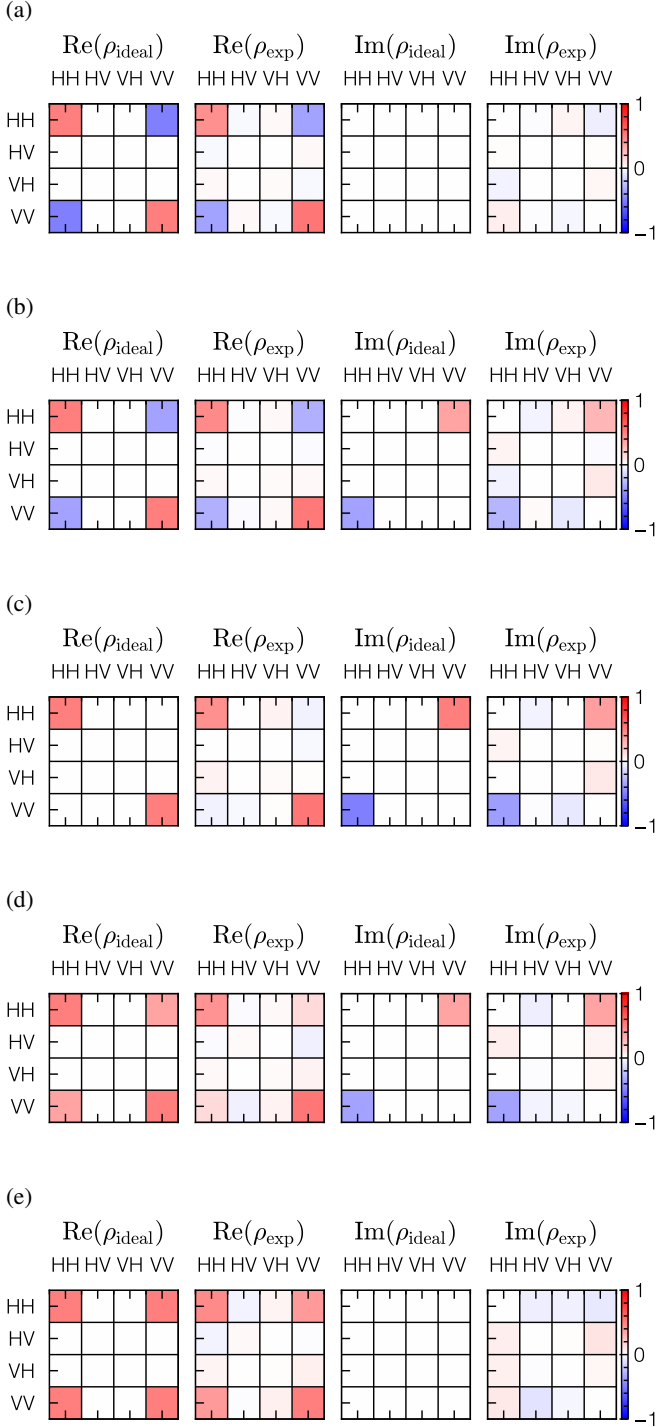


FIG. 3: Real and imaginary parts of the reconstructed density matrices for the state  $(|H_1, H_2\rangle - e^{i\phi'} |V_1, V_2\rangle)/\sqrt{2}$  where  $\phi'$  takes on the values **(a)**  $\phi' = 0$ , **(b)**  $\phi' = \pi/4$ , **(c)**  $\phi' = \pi/2$ , **(d)**  $\phi' = 3\pi/4$ , and **(e)**  $\phi' = \pi$ , respectively. All the density matrices are obtained using a maximum likelihood estimation (MLE) that takes the photon counts collected over a 10-second interval for each of the 16 projective measurements in Tab. C.1.

Fig. 3 shows reconstructed density matrices for the intermediate state  $(|H_1, H_2\rangle - e^{i\phi'} |V_1, V_2\rangle)/\sqrt{2}$  for the phases  $\phi' = 0, \pi/4, \pi/2, 3\pi/4$ , and  $\pi$ . On average, the fidelities for each state were found to be  $F(\rho_{\text{ideal}}, \rho_{\text{exp}}) = 0.8456 \pm 0.0140, 0.9041 \pm 0.0153, 0.8635 \pm 0.0130, 0.8335 \pm 0.0190$ , and  $0.8754 \pm 0.0184$ , respectively.

### C. Weighted graph state tomography

We now reconstruct the density matrices for the weighted graph state in Eq. 6 for specific targeted values of the graph weight  $\phi_{12}$ . This state is obtained by setting the HWPs in  $l_2$  and  $r_2$  to  $22.5^\circ$ , and for a graph weight  $\phi_{12}$ , the  $R_z(\phi'_{12})$  rotation in  $l_2$  is configured such that  $\phi'_{12} = \phi_{12} - \pi$ . Moreover, for each graph weight  $\phi_{12}$ , we have to ensure that the relative phase difference  $\varphi'$  between the paths  $l_2$  and  $r_2$  in the MZI in Fig. 1 equals  $\phi'_{12}/2 - \pi$ , such that the relative phase  $\varphi$  in Eq. 5 equals zero. This is done by monitoring the photon counts for the projector  $\hat{P}_1 \otimes \hat{P}_2 = |D_1\rangle \langle D_1| \otimes |H_2\rangle \langle H_2|$ . The detection probability for this projective measurement is given by,

$$P(o_1 = D_1, o_2 = H_2) = (1 + \cos \varphi)/2. \quad (10)$$

The above detection probability reaches a maximum when the aforementioned condition  $\varphi' = \phi'_{12}/2 - \pi$  is satisfied. This is the required condition for realizing a weighted graph state with weight  $\phi_{12}$  in Eq. 6. Thus, for a fixed weight  $\phi_{12}$ , we begin by fixing the rotation angle of the  $R_z(\phi'_{12})$  rotation to  $\phi'_{12} = \phi_{12} + \pi$  and vary  $\varphi'$  by translating the mirror in  $l_2$  until we observe a maximum number of coincidences for the projective measurement, which effectively sets  $\varphi = 0$  and consequently  $\varphi' = \phi'_{12}/2 - \pi$ . For our reconstruction, we target the weighted graph state when the graph weights  $\phi_{12}$  take on the values  $\phi_{12} = 0, \pi/4, \pi/2, 3\pi/4$  and  $\pi$ . Similarly here, when performing projective measurements we checkpoint the maximum photon counts and correct for any drift by translating the mirror inside  $l_2$  until we recover the checkpoint value.

Fig. 4 shows reconstructed density matrices for the weighted graph states  $|\Gamma_{\phi_{12}}\rangle$  where the weights take on the values  $\phi_{12} = 0, \pi/4, \pi/2, 3\pi/4$ , and  $\pi$ . On average, the fidelities for each state were found to be  $F(\rho_{\text{ideal}}, \rho_{\text{exp}}) = 0.8133 \pm 0.0156, 0.8134 \pm 0.0190, 0.8302 \pm 0.0178, 0.7943 \pm 0.0128$  and  $0.8349 \pm 0.0104$ , respectively. When the graph weight  $\phi_{12}$  takes on the value  $\pi$ , we recover the standard maximally-entangled two-qubit graph state, i.e.,  $|\Gamma_\pi\rangle = (|H_1, D_2\rangle + |V_1, A_2\rangle)/\sqrt{2}$ , our reconstructed density matrix at this weight has a concurrence of  $C = 0.780 \pm 0.229$ , indicative of the presence of entanglement [78–80]. As we decrease the weight towards zero, the concurrence of the reconstructed density matrices decreases all the way down to  $C = 0.0895 \pm 0.0152$ , indicative of a state close to a separable state. Indeed, the graph weight  $\phi_{12} = 0$  leads to the ideal product state  $|\Gamma_0\rangle = |D_1\rangle \otimes |D_2\rangle$ , which has a concurrence of zero.

## IV. QUANTUM SENSING

## A. Phase encoding

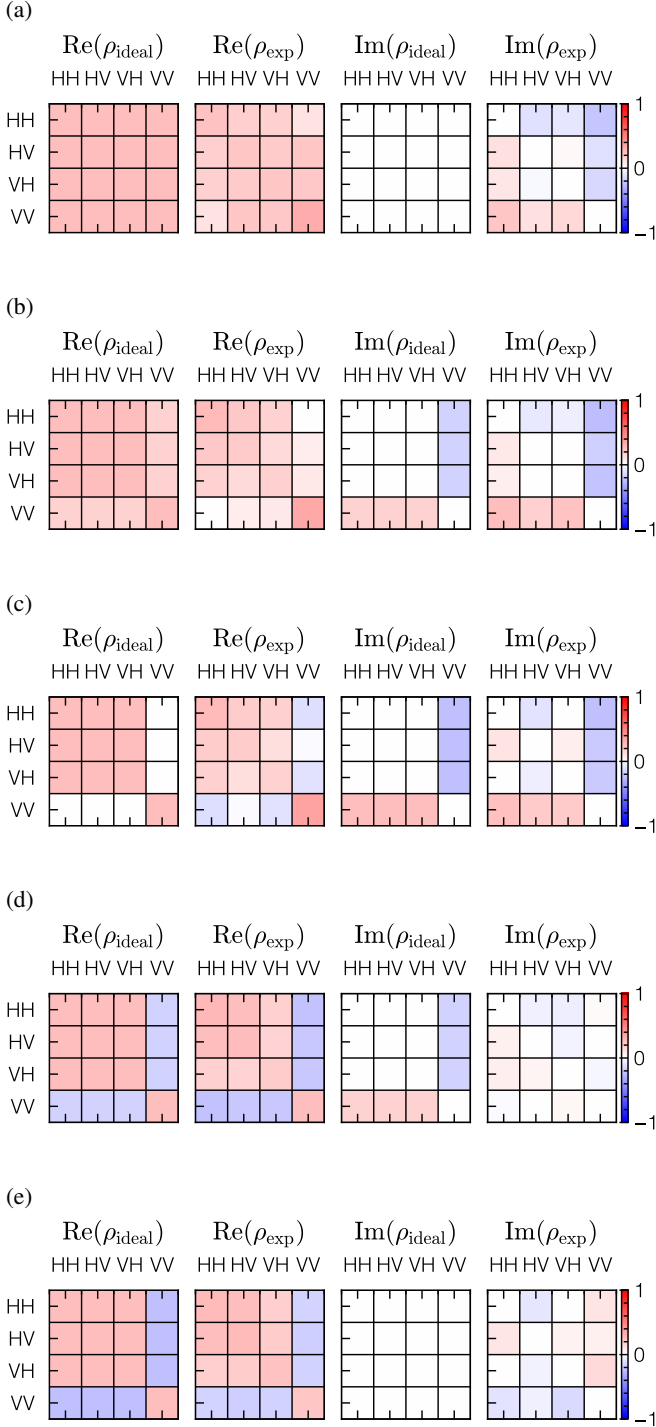


FIG. 4: Real and imaginary parts of the reconstructed density matrices for the weighted graph states  $(|H_1, D_2\rangle + |V_1, D_2^{\phi_{12}}\rangle)/\sqrt{2}$  where  $\phi_{12}$  takes on the values **(a)**  $\phi_{12} = 0$ , **(b)**  $\phi_{12} = \pi/4$ , **(c)**  $\phi_{12} = \pi/2$ , **(d)**  $\phi_{12} = 3\pi/4$ , and **(e)**  $\phi_{12} = \pi$ , respectively. All the density matrices are obtained using a maximum likelihood estimation (MLE) that takes the photon counts collected over 10 seconds interval for each of the 16 projective measurements in Tab. C.1.

Having characterized the generated weighted graph states  $|\Gamma_{\phi_{12}}\rangle$  for a range of graph weights, we study utilizing them as a resource for quantum metrology. Here, we leverage the generated states to probe a phase  $\theta$  with the primary objective of achieving the maximum measurement precision offered by the state at each graph weight  $\phi_{12}$ . Similar to Ref. [60], the scalar parameter  $\theta$  is encoded in the state  $\rho = |\Gamma_{\phi_{12}}\rangle\langle\Gamma_{\phi_{12}}|$  by a unitary transformation  $U(\theta)$  due to a Hamiltonian  $\hat{H}$

$$\rho \mapsto \rho_{\theta} := U(\theta)\rho U^{\dagger}(\theta), \quad \text{where } U(\theta) = e^{-i\hat{H}\theta/\hbar}. \quad (11)$$

The unitary operator represents the sensing process, and the parameter  $\theta$  dictates the strength or duration of an interaction represented by a Hamiltonian operator  $\hat{H}$ . Given this, we seek to determine the estimator variance  $(\Delta\theta)^2$  for an unbiased estimator  $\hat{\theta}$  of  $\theta$ ,

$$(\Delta\theta)^2 = \frac{(\Delta A)^2}{|\partial_{\theta}\langle\hat{A}\rangle|^2}, \quad (12)$$

where  $(\Delta A)^2 := \langle\hat{A}^2\rangle - \langle\hat{A}\rangle^2$  is the variance of the observable  $\hat{A}$ , and  $\langle\hat{A}\rangle$  is the expectation value of  $\hat{A}$ . To achieve the minimum estimator variance in  $\hat{\theta}$ , we should pick an observable  $\hat{A}$  that has a intrinsically low variance (numerator) and high sensitivity to changes in  $\theta$  (denominator). For separable states, the estimator variance  $(\Delta\theta)^2$  is bounded from below by the so-called standard quantum limit (SQL), which for an  $N$ -qubit state, scales asymptotically as  $\mathcal{O}(1/N)$ . On the other hand, for entangled states, the bound on  $(\Delta\theta)^2$  scales asymptotically as  $\mathcal{O}(1/N^2)$ , which is the so-called Heisenberg limit (HL) [11].

Given a quantum state  $\rho$  and a Hamiltonian  $\hat{H}$  generating the encoding unitary  $U(\theta)$ , when there are no restrictions on the choice for  $\hat{A}$ , minimizing the expression in Eq. 12 over all possible quantum measurement observables, i.e., positive operator-value measures (POVMs), recovers the smallest achievable single-shot variance  $(\Delta\theta)^2$  for  $\rho$  and  $\hat{H}$ , known as the quantum Cramér-Rao bound (QCRB) [81–84]

$$(\Delta\theta)^2 \geq \frac{1}{F_Q(\rho, \hat{H})}. \quad (13)$$

Here,  $F_Q$  is the quantum Fisher information (QFI) [83, 85], which quantifies the state's sensitivity to small variations in  $\theta$ . In this study, we consider a Hamiltonian  $\hat{H}$  that takes form

$$\hat{H} = (\hat{X}_1 \otimes \mathbf{1}_2 + \mathbf{1}_1 \otimes \hat{Z}_2)/2, \quad (14)$$

which is a locally rotated version of  $\hat{H}$  used for the Bell state  $|\Phi^{(+)}\rangle$ , as  $|\Gamma_{\pi}\rangle = (H \otimes \mathbf{1})|\Phi^{(+)}\rangle$  [86]. The unitary transformation then becomes:

$$U(\theta) = e^{-i\hat{H}\theta/\hbar} = R_x^{(1)}(\theta) \otimes R_z^{(2)}(\theta). \quad (15)$$

In our experiment, this unitary is realized through a configuration of a QWP-HWP-QWP chain; one set for  $R_x(\theta)$  and another for  $R_z(\theta)$  (see Fig. 1). By changing the waveplate angles we can target an arbitrary value for the phase  $\theta$ . Appendix A gives the relation between  $\theta$  and the waveplate angles. Practically, we should operate at a point where the observable's expectation value has the steepest gradient, i.e., highest sensitivity to changes in  $\theta$ . Theoretically, the QFI for the 2-qubit weighted graph state, encoded via the unitary operator in Eq. 15 depends only on the graph weight  $\phi_{12}$  and is independent of the encoded phase  $\theta$  (see Appendix D for the derivation). We fix the sensing phase at  $\theta = 0$ , as small  $\theta$  represents the most interesting regimes for quantum metrology and its advantage over classical methods. This choice does not limit generality, as any arbitrary phase  $\theta$  can be shifted to this operating point via an offset phase and we are ultimately interested not in  $\theta$  but in the precision  $(\Delta\theta)^2$  around  $\theta$ .

### B. Estimator variance for local Pauli measurements

To experimentally evaluate the metrological performance of our weighted graph states  $|\Gamma_{\phi_{12}}\rangle$ , we experimentally determine the estimator variance  $(\Delta\theta)^2$  in Eq. 12 by measuring a set of observable operators  $\hat{A}$ . We test two distinct sets of local measurements, progressively relaxing the constraints dictated by our experimental setup. Initially, we restrict the observable  $\hat{A}$  to be a tensor product of single-qubit Pauli operators  $\hat{A} = \hat{A}_1 \otimes \hat{A}_2$ , where  $\hat{A}_i \in \{\mathbb{1}, \hat{X}, \hat{Y}, \hat{Z}\}$ . The corresponding measurement bases for these are products of the three standard single-photon bases: rectilinear basis  $\{|H\rangle, |V\rangle\}$ , diagonal basis  $\{|D\rangle, |A\rangle\}$  and circular basis  $\{|R\rangle, |L\rangle\}$ . We perform an exhaustive numerical search over all  $4^2 = 16$  possible local Pauli product operators at each graph weight  $\phi_{12}$  to find the operator  $\hat{A}$  that yields the smallest value for  $(\Delta\theta)^2$ . In cases where multiple operators achieve the same minimum variance, we select the one with the largest gradient magnitude  $|\partial_\theta \langle \hat{A} \rangle|$ , as this is generally preferred for robust experimental implementation. More information about the optimal local Pauli operators at the graph weights of interest, when  $\theta = 0$ , can be found in Appendix E.

To determine the estimator variance for each graph weight  $\phi_{12}$  of interest given an optimal observable operator  $\hat{A}$ , we begin by evaluating the single-shot variance  $(\Delta A)^2 = 1 - \langle \hat{A} \rangle^2$  at  $\theta = 0$ . This is done by first collecting photon coincidence counts  $N_{\square\square}$  for each of the four projective measurements of  $\hat{A}$ , i.e.,  $N_{++}$ ,  $N_{+-}$ ,  $N_{-+}$ , and  $N_{--}$ . Each of the photon counts are collected over a 10-second interval, and we build up data sets of six samples for each projective measurement. The single-shot variance  $(\Delta A)^2 = 1 - \langle \hat{A} \rangle^2$  is then calculated via a non-parametric bootstrap resampling method [87] on the data set. More information about the bootstrapping method can be found in Appendix F. The values of  $(\Delta A)^2$  for a range of weights are shown in Fig. 5a, where there is a degree of correlation between the experiment and the ideal case.

It is important to note that  $(\Delta A)^2$  is the noise originating from quantum fluctuations only for a single pair of entangled photons in the state  $|\Gamma_{\phi_{12}}\rangle$ . However, in our experiment we are measuring coincidence counts corresponding to many pairs of entangled photons over a fixed period of 10 seconds, where the number of shots (photon pairs) fluctuates due to Poisson noise from the SPDC process. This results in additional noise in the data. In Appendix F we show that for large mean coincidence counts, the impact of Poisson noise on the measured value of  $(\Delta A)^2$  is negligible, giving the value that can be expected if one were to do sensing shot-by-shot. One way to do this is to detect both outputs of the PBSs in the experiment and reduce the integration time from 10 secs to approximately the inverse of the count rate.

Each state's sensitivity  $|\partial_\theta \langle \hat{A} \rangle|$  is also measured around the operating point  $\theta = 0$ . The exact derivative for our phase encoding unitary in Eq. 15 can be evaluated via the parameter-shift rule [88]. However, to reduce the number of required measurements, we approximate the derivative using a 2-point finite difference method with a fixed shift  $h = 5^\circ$ .

$$\partial_\theta \langle \hat{A} \rangle \Big|_{\theta=\theta^*} \approx \frac{\langle \hat{A} \rangle(\theta^* + h) - \langle \hat{A} \rangle(\theta^* - h)}{2h}, \quad (16)$$

where the argument  $(\theta \pm h)$  implies the rotation  $U(\theta \pm h) = R_x^{(1)}(\theta \pm h) \otimes R_z^{(2)}(\theta \pm h)$ . This approach requires only two experimental evaluations of  $\langle \hat{A} \rangle$  around the point of interest  $\theta^*$ , and has truncation error of order  $\mathcal{O}(h^2)$ . This is a pragmatic choice, as the parameter-shift rule would require four evaluations of  $\langle \hat{A} \rangle$ , which requires more stringent conditions on the stability of  $\varphi'$  in our experiment.

Similar to the observable variance, the observable derivative in Eq. 16 is calculated with a non-parametric bootstrap resampling method from the 6-sample data sets of the projective measurements for  $\langle \hat{A} \rangle$  at  $\theta = -5^\circ$  and  $\theta = 5^\circ$ . These results are shown Fig. 5b and show reasonable agreement between the experiment and ideal case. Further details about the optimal local Pauli operators for each graph weight can be found in Appendix E. Finally, to evaluate the estimator variance  $(\Delta\theta)^2$  we combine the three data sets for  $\langle \hat{A} \rangle$ , at  $\theta = \{-5^\circ, 0^\circ, 5^\circ\}$  and bootstrap the data sets to calculate the estimator variance  $(\Delta\theta)^2$  in Eq. 12. The results of this are shown in Fig. 6. We observe a close quantitative agreement between the experimental results and theoretical predictions. For the graph weights  $\phi_{12} = \pi, 7\pi/8, 3\pi/4$ , and  $5\pi/8$ , the experimental estimator variance  $(\Delta\theta)^2$  is well below the SQL, highlighting a gain in precision even for non-optimal graph weights  $\pi > \phi_{12} \geq 5\pi/8$ , which correspond to non-maximally-entangled states. The data point for  $\phi_{12} = \pi/4$  is an outlier, potentially due to the observable derivative being smallest in magnitude  $\sim 0.85$  (theory), thus the most susceptible to experimental errors.

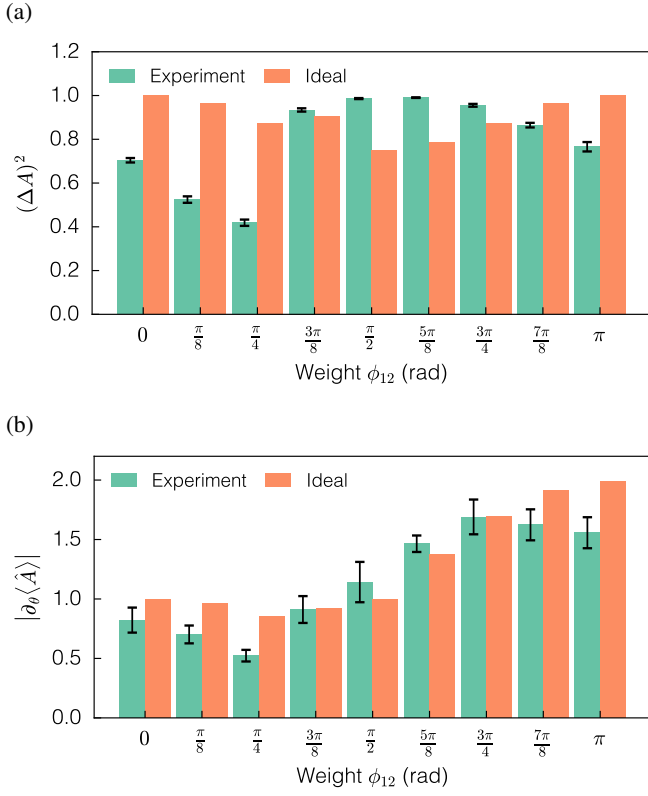


FIG. 5: **(a)** Single-shot observable variance  $(\Delta A)^2$ , and **(b)** magnitude of the observable derivative  $|\partial_\theta \langle \hat{A} \rangle|$ , measured via a 2-point finite difference method for the optimal local Pauli measurements as a function of the graph weight  $\phi_{12}$  for the sensing phase  $\theta = 0$ . The errors represent 95% confidence intervals for the respective quantities.

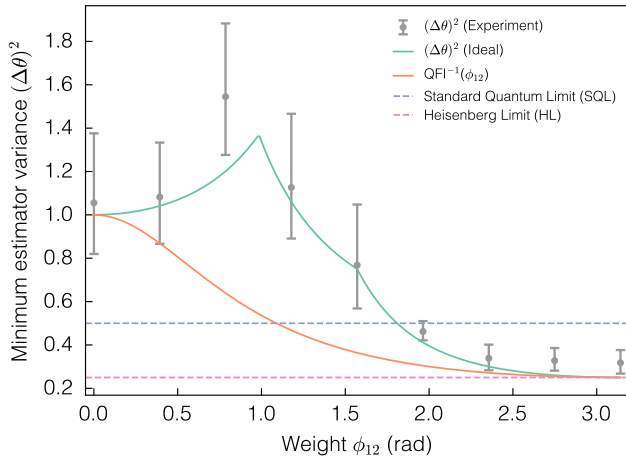


FIG. 6: The estimator variance  $(\Delta\theta)^2$  for the optimal local Pauli measurements. The grey dashed horizontal line represents the standard quantum limit (SQL), where  $(\Delta\theta)^2 = 1/2$ . The pink dashed horizontal line represents the Heisenberg limit (HL),  $(\Delta\theta)^2 = 1/4$ . The errors represent 95% confidence intervals of the bootstrap samples for the respective quantities.

### C. Estimator variance for local general-axis measurements

We now relax the constraint on the measurements, allowing  $\hat{A}$  to be any general-axis local operator, corresponding to a projective measurement along an arbitrary direction  $(\beta_i, \alpha_i)$  on the Bloch sphere for each qubit ( $i = 1, 2$ ). The observable  $\hat{A}$  takes the form:

$$\hat{A} = \hat{A}_1(\beta_1, \alpha_1) \otimes \hat{A}_2(\beta_2, \alpha_2),$$

$$\hat{A}_i(\beta_i, \alpha_i) := |\beta_i, \alpha_i, +\rangle\langle\beta_i, \alpha_i, +| - |\beta_i, \alpha_i, -\rangle\langle\beta_i, \alpha_i, -|. \quad (17)$$

Here, the projectors are formed from the general-axis basis states, given by

$$|\beta, \alpha, +\rangle := \cos(\beta/2) |0\rangle + \sin(\beta/2)e^{i\alpha} |1\rangle,$$

$$|\beta, \alpha, -\rangle := -\sin(\beta/2) |0\rangle + \cos(\beta/2)e^{i\alpha} |1\rangle, \quad (18)$$

where  $\beta$  and  $\alpha$  are the polar and azimuthal angles, respectively. We use this parameterization to perform numerical optimization for each graph weight  $\phi_{12}$  to find the optimal set of angles  $\{\beta_1, \alpha_1, \beta_2, \alpha_2\}$  that minimize  $(\Delta\theta)^2$ . To guide the search towards experimentally robust optima, a soft penalty is added to encourage solutions with a large gradient magnitude. Experimentally, these general-axis measurements can be realized by setting specific angles for the HWP and QWP acting on each photon at the measurement stage. The wave plate angles are derived from the optimal polar and azimuthal angles  $\{(\beta_i, \alpha_i)\}$  by another numerical optimization routine (see Appendix G for more details). To experimentally evaluate the estimator variance for each graph weight  $\phi_{12}$  of interest given an optimal general-axis measurement, we follow the same procedure as in the local Pauli measurements; we collect data sets of the projective measurements for  $\langle \hat{A} \rangle$ , at  $\theta = \{-5^\circ, 0^\circ, 5^\circ\}$  and bootstrap the data sets to calculate the observable variance, observable derivative, and estimator variance  $(\Delta\theta)^2$  in Eq. 12.

The comparison between the experimental and ideal observable variance  $(\Delta A)^2$  and sensitivity  $|\partial_\theta \langle \hat{A} \rangle|$  at  $\theta = 0$  for the optimal local general-axis operators for each graph weight  $\phi_{12}$  are shown in Fig. 7a and Fig. 7b, respectively. As with the local Pauli measurements, one can see a reasonable agreement between the experimental and ideal cases. Fig. 8 compares the experimental and ideal estimator variance  $(\Delta\theta)^2$  for local general-axis measurements. Once again, there is a close degree of quantitative agreement between experimental results and theoretical predictions. Using general-axis measurements has the effect of bringing the estimator variance closer to the QCRB. Moreover, in contrast to the local Pauli measurements, there is a larger range of graph weights that are below the SQL ( $\pi \geq \phi_{12} \geq \pi/2$ ); the data point at  $\phi_{12} = \pi/2$  has now been pushed below the SQL.

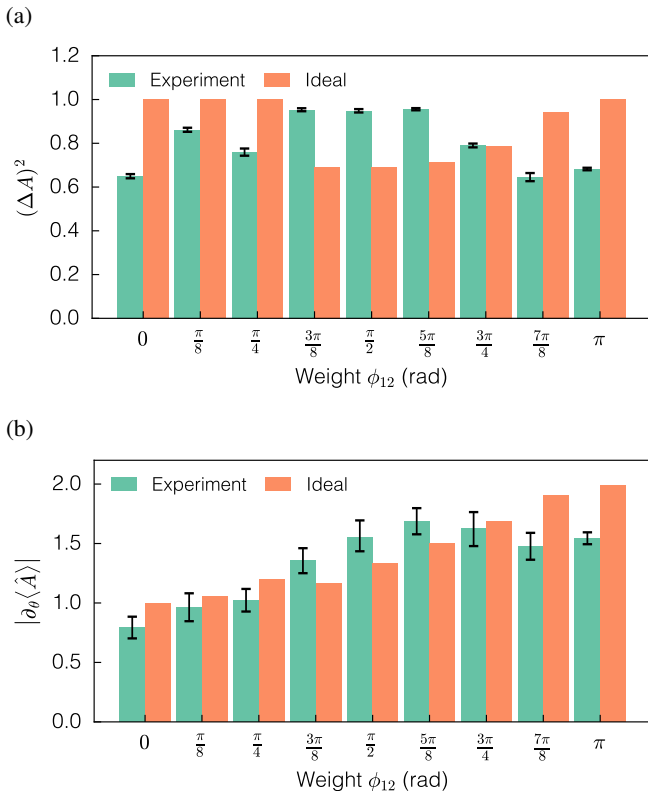


FIG. 7: **(a)** Single-shot observable variance  $(\Delta A)^2$ , and **(b)** magnitude of the observable derivative  $|\partial_\theta \langle \hat{A} \rangle|$  measured via a 2-point finite difference method for the optimal local general-axis measurements as a function of the graph weight  $\phi_{12}$  for the sensing phase  $\theta = 0$ . The errors represent 95% confidence intervals of the bootstrap samples for the respective quantities.

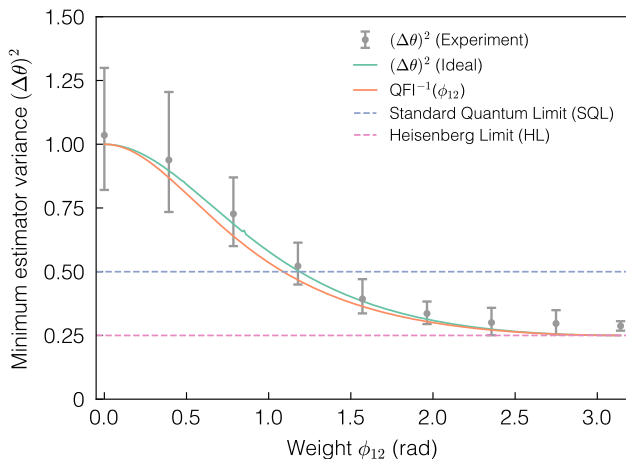


FIG. 8: The estimator variance  $(\Delta\theta)^2$  for the optimal local general-axis measurements. The grey dashed horizontal line represents the SQL,  $(\Delta\theta)^2 = 1/2$ . The pink dashed horizontal line represents the HL,  $(\Delta\theta)^2 = 1/4$ . The errors represent 95% confidence intervals for the respective quantities.

## D. Practical considerations

The systematic mismatch between the experimentally measured values and the theoretical predictions in Fig. 5 and Fig. 7 can be explained by an effective offset in the implemented graph weight and by small miscalibrations in the waveplates used to realize the encoding unitary. In the experiment, the weight  $\phi_{12}$  is set by an interferometer and is therefore sensitive to residual phases in each path and to slow drifts during data acquisition; the reconstructed density matrices in Fig. 4 and their corresponding fidelities already highlight this effect. Importantly, while a QWP-HWP-QWP configuration implements the intended single-qubit operation up to an overall (global) phase, any *path-dependent* phase introduced by the optical elements appears as an additional relative phase between interferometer arms and therefore shifts the effective graph weight, i.e.  $\phi_{12} \mapsto \phi_{12}^{\text{eff}}$ . For example, the QWP-HWP-QWP configuration used to implement the identity operation in path  $r_2$  is equivalent to the identity only up to a constant phase factor (here  $e^{\pm i\pi/2}$ ); when this phase is not common to both paths it contributes directly to the relative arm phase. In addition, the effective rotation axes and zero-angle references of the QWP-HWP-QWP configurations used to realize the identity operation for photon 2 in  $r_2$ ,  $R_z(\varphi'_{12})$  for photon 2 in  $l_2$ , and the encoding rotations  $R_x(\theta)$  for photon 1 and  $R_z(\theta)$  for photon 2 can be shifted by small mounting and calibration offsets. Consequently, these systematic shifts in the graph weight and in the realized encoding unitary manifest predominantly as deviations in the measured observable derivative and variance.

## V. CONCLUSION

In summary, we have demonstrated a proof-of-concept scheme for realizing a photonic two-qubit weighted graph state with an arbitrarily tunable weight, using linear optics and a single polarization-entangled photon-pair source based on SPDC. We successfully generated weighted graph states with different weights with a fidelity in excess of 80%. Following the theoretical framework in Ref. [60], establishing the robustness of weighted graph states for metrological applications, we experimentally verified that considerably less entanglement is required to achieve a quantum advantage for metrology. In the first case, this was done by experimentally verifying that under local Pauli measurements, weighted graph states with  $\pi \geq \phi_{12} \geq 5\pi/8$  are sufficient to yield a gain in precision beyond the SQL. Relaxing the restriction and allowing local measurements along an arbitrary axis led to a wider range of graph weights  $\pi \geq \phi_{12} \geq \pi/2$  that correspond to weighted graph states achieving a gain in precision below the SQL.

Our results highlight the practical utility of weighted graph states by demonstrating that near-maximal entanglement is not a prerequisite for achieving quantum-enhanced sensing. This is important for real-world applications where noise and decoherence often limit the generation and maintenance of highly entangled states. By showing that mod-

erate levels of entanglement ( $\phi_{12} \geq \pi/2$ ) are sufficient to surpass the classical limit, our work reflects a resource-efficient route to quantum metrology. The experimental results presented here were achieved with weighted graph states with fidelities in excess of 80%. We anticipate that the fidelity of the generated weighted graph states can be significantly improved via standard methods, such as utilizing high-efficiency entangled-photon sources, implementing spectral mode matching, and using walk-off compensators for temporal matching of horizontally- and vertically-polarized light cones emitted by the cascaded BBOs [89–91]. These improvements could potentially have direct downstream effects, resulting in an improved measured estimator variance  $(\Delta\theta)^2$ .

Directions for future work include extending this generation scheme to larger systems, building upon established methods for standard graph states such as those presented in Ref. [31, 64]. The use of moderately sized weighted graph states could be immediately beneficial for quantum computing paradigms like fusion-based quantum computation [6, 7], as weighted states are already known to increase the success

probability for the fusion process [58]. Beyond scaling the resource state, the metrology protocol itself could be enhanced in two primary ways. First, it could be extended to multiparameter estimation [92–95], where the encoding unitary possesses two or more independent parameters instead of one, such as simultaneously sensing the  $x$  and  $y$  components of a magnetic or electric field [96–99]. Second, the protocol could be automated for larger weighted graph states and/or multiple parameters via an end-to-end variational framework for quantum sensing protocols [97, 98, 100].

## ACKNOWLEDGMENTS

This research was supported by the South African National Research Foundation, the South African Council for Scientific and Industrial Research, and the South African Department of Science and Innovation through its Quantum Initiative program (SAQuTI).

- 
- [1] H. J. Briegel and R. Raussendorf, *Physical Review Letters* **86**, 910–913 (2001).
  - [2] R. Raussendorf and H. J. Briegel, *Physical Review Letters* **86**, 5188 (2001).
  - [3] R. Raussendorf, D. E. Browne, and H. J. Briegel, *Physical Review A* **68**, 022312 (2003).
  - [4] P. Walther *et al.*, *Nature* **434**, 169–176 (2005).
  - [5] N. C. Menicucci *et al.*, *Physical Review Letters* **97**, 110501 (2006).
  - [6] S. Bartolucci *et al.*, *Nature Communications* **14**, 912 (2023).
  - [7] P. Thomas, L. Ruscio, O. Morin, and G. Rempe, *Nature* **629**, 567–572 (2024).
  - [8] W. Dür, H. Aschauer, and H.-J. Briegel, *Physical Review Letters* **91**, 107903 (2003).
  - [9] D. Markham and B. C. Sanders, *Physical Review A* **78**, 042309 (2008).
  - [10] N. Friis *et al.*, *New Journal of Physics* **19**, 063044 (2017).
  - [11] N. Shettell and D. Markham, *Physical Review Letters* **124**, 110502 (2020).
  - [12] C. Song *et al.*, *Physical Review Letters* **119**, 180511 (2017).
  - [13] G. J. Mooney, C. D. Hill, and L. C. L. Hollenberg, *Scientific Reports* **9**, 13465 (2019).
  - [14] P. Thomas, L. Ruscio, O. Morin, and G. Rempe, *Nature* **608**, 677–681 (2022).
  - [15] B. P. Lanyon *et al.*, *Physical Review Letters* **111**, 210501 (2013).
  - [16] I. Pogorelov *et al.*, *PRX Quantum* **2**, 020343 (2021).
  - [17] S. A. Moses *et al.*, *Physical Review X* **13**, 041052 (2023).
  - [18] M. Ringbauer *et al.*, *Nature Communications* **16**, 106 (2025).
  - [19] H. Kang, J. F. Kam, G. J. Mooney, and L. C. L. Hollenberg, *Scientific Reports* **10.1038/s41598-025-30301-0** (2025).
  - [20] O. Mandel *et al.*, *Nature* **425**, 937–940 (2003).
  - [21] J. Cramer *et al.*, *Nature Communications* **7**, 11526 (2016).
  - [22] D. Istrati *et al.*, *Nature Communications* **11**, 5501 (2020).
  - [23] D. Cogan, Z.-E. Su, O. Kenneth, and D. Gershoni, *Nature Photonics* **17**, 324 (2023).
  - [24] H. Huet *et al.*, *Nature Communications* **16**, 4337 (2025).
  - [25] J. L. O’Brien, *Science* **318**, 1567 (2007).
  - [26] J. Wang, F. Sciarrino, A. Laing, and M. G. Thompson, *Nature Photonics* **14**, 273–284 (2019).
  - [27] H.-S. Zhong *et al.*, *Science* **370**, 1460 (2020).
  - [28] D. E. Browne and T. Rudolph, *Physical Review Letters* **95**, 010501 (2005).
  - [29] W.-B. Gao *et al.*, *Nature Physics* **6**, 331–335 (2010).
  - [30] J.-P. Li *et al.*, *ACS Photonics* **7**, 1603 (2020).
  - [31] H. S. Park, J. Cho, J. Y. Lee, D.-H. Lee, and S.-K. Choi, *Optics Express* **15**, 17960 (2007).
  - [32] S. M. Lee *et al.*, *Optics Express* **20**, 6915 (2012).
  - [33] X.-L. Wang *et al.*, *Physical Review Letters* **120**, 260502 (2018).
  - [34] H.-S. Zhong *et al.*, *Physical Review Letters* **121**, 250505 (2018).
  - [35] J. Bao *et al.*, *Nature Photonics* **17**, 573 (2023).
  - [36] M. Pont *et al.*, *npj Quantum Information* **10**, 50 (2024).
  - [37] Z. Wang *et al.*, *Light: Science & Applications* **14**, 164 (2025).
  - [38] Y. Yang *et al.*, *npj Quantum Information* **11**, 19 (2025).
  - [39] O. Firstenberg *et al.*, *Nature* **502**, 71 (2013).
  - [40] O. Firstenberg, C. S. Adams, and S. Hofferberth, *Journal of Physics B: Atomic, Molecular and Optical Physics* **49**, 152003 (2016).
  - [41] D. Tiarks, S. Schmidt, G. Rempe, and S. Dür, *Science Advances* **2**, e1600036 (2016).
  - [42] J. D. Thompson *et al.*, *Nature* **542**, 206 (2017).
  - [43] D. Tiarks, S. Schmidt-Eberle, T. Stolz, G. Rempe, and S. Dür, *Nature Physics* **15**, 124–126 (2018).
  - [44] S. Sagona-Stopfel, R. Shahrokhshahi, B. Jordaan, M. Namazi, and E. Figueroa, *Physical Review Letters* **125**, 243601 (2020).
  - [45] V. S. Ferreira, G. Kim, A. Butler, H. Pichler, and O. Painter, *Nature Physics* **20**, 865 (2024).
  - [46] A. B. Young *et al.*, *Physical Review A* **84**, 011803 (2011).
  - [47] Z. Qin and V. W. Scarola, *Physical Review A* **111**, 042617 (2025).
  - [48] J. O’Sullivan *et al.*, *Nature Communications* **16**, 5505 (2025).
  - [49] W. Dür, L. Hartmann, M. Hein, M. Lewenstein, and H.-J. Briegel, *Physical Review Letters* **94**, 097203 (2005).
  - [50] M. Hein *et al.*, (2006), arXiv:quant-ph/0602096 [quant-ph].

- [51] L. Hartmann, J. Calsamiglia, W. Dür, and H. J. Briegel, *Journal of Physics B: Atomic, Molecular and Optical Physics* **40**, S1 (2007).
- [52] S. Anders, M. B. Plenio, W. Dür, F. Verstraete, and H.-J. Briegel, *Physical Review Letters* **97**, 107206 (2006).
- [53] S. Anders, H. J. Briegel, and W. Dür, *New Journal of Physics* **9**, 361 (2007).
- [54] A. D. K. Plato, O. C. Dahlsten, and M. B. Plenio, *Physical Review A* **78**, 042332 (2008).
- [55] M. S. Tame, Ş. K. Özdemir, M. Koashi, N. Imoto, and M. S. Kim, *Physical Review A* **79**, 020302 (2009).
- [56] M. Hayashi and Y. Takeuchi, *New Journal of Physics* **21**, 093060 (2019).
- [57] D. Ghosh, K. Das Agarwal, P. Halder, and A. Sen(De), *Physical Review A* **110**, 022431 (2024).
- [58] N. Rimock, K. Cohen, and Y. Oz, (2024), [arXiv:2406.15666](https://arxiv.org/abs/2406.15666) [quant-ph].
- [59] P. Xue, *Physical Review A* **86**, 023812 (2012).
- [60] B. J. Alexander, S. K. Ozdemir, and M. S. Tame, (2026), [arXiv:2602.13026](https://arxiv.org/abs/2602.13026) [quant-ph].
- [61] N. Paunković, Y. Omar, S. Bose, and V. Vedral, *Physical Review Letters* **88**, 187903 (2002).
- [62] Z. Zhao, T. Yang, Y.-A. Chen, A.-N. Zhang, and J.-W. Pan, *Physical Review Letters* **90**, 207901 (2003).
- [63] M.-J. Hwang and Y.-H. Kim, *Physics Letters A* **369**, 280 (2007).
- [64] W. Xiong and L. Ye, *Journal of the Optical Society of America B* **28**, 2030 (2011).
- [65] Y.-B. Sheng, L. Zhou, S.-M. Zhao, and B.-Y. Zheng, *Physical Review A* **85**, 012307 (2012).
- [66] F.-G. Deng, *Physical Review A* **85**, 022311 (2012).
- [67] L. Zhou, Y.-B. Sheng, W.-W. Cheng, L.-Y. Gong, and S.-M. Zhao, *Journal of the Optical Society of America B* **30**, 71 (2012).
- [68] B. S. Choudhury and A. Dhara, *Quantum Information Processing* **12**, 2577 (2013).
- [69] X. Li and S. Ghose, *Laser Physics Letters* **11**, 125201 (2014).
- [70] R. Frantzeskakis, C. Liu, Z. Raissi, E. Barnes, and S. E. Economou, *Physical Review Research* **5**, 023124 (2023).
- [71] P. G. Kwiat, E. Waks, A. G. White, I. Appelbaum, and P. H. Eberhard, *Physical Review A* **60**, R773–R776 (1999).
- [72] R. Simon and N. Mukunda, *Physics Letters A* **143**, 165 (1990).
- [73] S. G. Reddy *et al.*, *Journal of the Optical Society of America A* **31**, 610 (2014).
- [74] M. H. M. Passos, A. d. O. Junior, M. C. de Oliveira, A. Z. Khoury, and J. A. O. Huguenin, *Physical Review A* **102**, 062601 (2020).
- [75] D. Branning, S. Bhandari, and M. Beck, *American Journal of Physics* **77**, 667 (2009).
- [76] M. A. Nielsen and I. L. Chuang, *Quantum Computation and Quantum Information: 10th Anniversary Edition*, 10th ed. (Cambridge University Press, USA, 2011).
- [77] D. F. V. James, P. G. Kwiat, W. J. Munro, and A. G. White, *Physical Review A* **64**, 052312 (2001).
- [78] S. A. Hill and W. K. Wootters, *Physical Review Letters* **78**, 5022 (1997).
- [79] G. Romero, C. E. López, F. Lastra, E. Solano, and J. C. Retamal, *Physical Review A* **75**, 032303 (2007).
- [80] R. Horodecki, P. Horodecki, M. Horodecki, and K. Horodecki, *Review of Modern Physics* **81**, 865 (2009).
- [81] C. W. Helstrom, *Journal of Statistical Physics* **1**, 231 (1969).
- [82] S. L. Braunstein and C. M. Caves, *Physical Review Letters* **72**, 3439 (1994).
- [83] M. G. A. Paris, *International Journal of Quantum Information* **07**, 125 (2009).
- [84] A. S. Holevo, *Probabilistic and Statistical Aspects of Quantum Theory*, Publications of the Scuola Normale Superiore. Monographs (Springer, Dordrecht, 2011).
- [85] D. Petz and C. Ghinea, in *Quantum Probability and Related Topics* (World Scientific, 2011).
- [86] G. Tóth and I. Apellaniz, *Journal of Physics A: Mathematical and Theoretical* **47**, 424006 (2014).
- [87] B. Efron and R. J. Tibshirani, *An introduction to the bootstrap*, Chapman & Hall/CRC monographs on statistics and applied probability (Chapman and Hall, London, 1993).
- [88] G. E. Crooks, (2019), [arXiv:1905.13311](https://arxiv.org/abs/1905.13311) [quant-ph].
- [89] J. B. Altepeter, E. R. Jeffrey, and P. G. Kwiat, *Optics Express* **13**, 8951 (2005).
- [90] G. M. Akselrod, J. B. Altepeter, E. R. Jeffrey, and P. G. Kwiat, *Optics Express* **15**, 5260 (2007).
- [91] R. Rangarajan, M. Goggin, and P. Kwiat, *Optics Express* **17**, 18920 (2009).
- [92] T. J. Proctor, P. A. Knott, and J. A. Dunningham, *Phys. Rev. Lett.* **120**, 080501 (2018).
- [93] W. Ge, K. Jacobs, Z. Eldredge, A. V. Gorshkov, and M. Foss-Feig, *Phys. Rev. Lett.* **121**, 043604 (2018).
- [94] Z. Zhang and Q. Zhuang, *Quantum Science and Technology* **6**, 043001 (2021).
- [95] D.-H. Kim *et al.*, *Nature Communications* **15**, 266 (2024).
- [96] R. Kaubruegger, A. Shankar, D. V. Vasilyev, and P. Zoller, *PRX Quantum* **4**, 020333 (2023).
- [97] M. Valeri *et al.*, *Physical Review Research* **5**, 013138 (2023).
- [98] T. K. Le, H. Q. Nguyen, and L. B. Ho, *Scientific Reports* **13**, 17775 (2023).
- [99] J. Zhang *et al.*, (2024), [arXiv:2412.18398](https://arxiv.org/abs/2412.18398) [quant-ph].
- [100] B. MacLellan, P. Roztocky, S. Czischek, and R. G. Melko, *npj Quantum Information* **10**, 118 (2024).

### Appendix A: Single-qubit rotation gates with polarization optics

A general SU(2) matrix can be written as a sequence of three rotations characterized by the Euler angles  $(\varphi, \xi, \zeta)$ ,

$$U(\varphi, \xi, \zeta) = \tilde{R}_y(\varphi)\tilde{R}_z(-\xi)\tilde{R}_y(\zeta), \quad (\text{A.1})$$

where  $\tilde{R}_{\hat{n}}(\psi) = e^{-i\psi\hat{n}\cdot\sigma}$ . Here  $\hat{n}$  is a unit vector and  $\sigma = (\sigma_x, \sigma_y, \sigma_z)$  are the Pauli matrices. Note that the  $\tilde{R}_{\hat{n}}(\psi/2) = R_{\hat{n}}(\psi)$ , where the latter is the standard definition [76]. For polarization-based operations, a general SU(2) operator can be decomposed as a product of waveplate operations in the following way:

$$U(\eta_1, \tau, \eta_2) = \text{QWP}(\eta_1)\text{HWP}(\tau)\text{QWP}(\eta_2) \quad (\text{A.2})$$

where

$$\begin{aligned} \text{QWP}(\eta) &= \tilde{R}_y(\eta)Q_0\tilde{R}_y(-\eta), \\ \text{HWP}(\tau) &= \tilde{R}_y(\tau)H_0\tilde{R}_y(-\tau), \\ Q_0 &= \begin{bmatrix} 1 & 0 \\ 0 & i \end{bmatrix}, \\ H_0 &= \begin{bmatrix} 1 & 0 \\ 0 & -1 \end{bmatrix}. \end{aligned} \quad (\text{A.3})$$

A simple relation can be established between the waveplates and the Euler angles [74]:

$$\begin{aligned} \eta_1 &= \varphi - \pi/4, \\ \eta_2 &= -\zeta - \pi/4, \\ \tau &= (\varphi + \xi - \zeta)/2 - \pi/4. \end{aligned} \quad (\text{A.4})$$

#### 1. Waveplate angles for x-axis rotation operator

We obtain  $R_x(\theta)$  by setting  $\varphi = -\pi/4$ ,  $\zeta = \pi/4$  and  $\xi = \theta/2$  in Eq. A.1 to give

$$U(-\pi/4, \theta/2, \pi/4) = \tilde{R}_y(-\pi/4)\tilde{R}_z(-\theta/2)\tilde{R}_y(\pi/4) = \tilde{R}_x(\theta/2) = R_x(\theta). \quad (\text{A.5})$$

The relation between the waveplate angles and  $\theta$  are given by

$$\begin{aligned} \eta_1 &= -\pi/2, \\ \eta_2 &= -\pi/2, \\ \tau &= \theta/4 - \pi/2. \end{aligned} \quad (\text{A.6})$$

#### 2. Waveplate angles for y-axis rotation operator

Similarly,  $R_y(\theta)$  can be obtained by setting  $\varphi = \xi = 0$  and  $\zeta = \theta/2$  in Eq. A.1 to give

$$U(0, 0, \theta/2) = \tilde{R}_y(0)\tilde{R}_z(0)\tilde{R}_y(\theta/2) = \tilde{R}_y(\theta/2) = R_y(\theta), \quad (\text{A.7})$$

where the waveplate angles are related to  $\theta$  via

$$\begin{aligned} \eta_1 &= -\pi/4, \\ \eta_2 &= -\theta/2 - \pi/4, \\ \tau &= -\theta/4 - \pi/4. \end{aligned} \quad (\text{A.8})$$

### 3. Waveplate angles for z-axis rotation operator

Setting  $\varphi = \zeta = 0$  and  $\xi = -\theta/2$ , Eq. A.1 becomes:

$$U(0, -\theta/2, 0) = \tilde{R}_y(0)\tilde{R}_z(\theta/2)\tilde{R}_y(0) = \tilde{R}_z(\theta/2) = R_z(\theta). \quad (\text{A.9})$$

The waveplate angles are related to  $\theta$  via

$$\begin{aligned} \eta_1 &= -\pi/4, \\ \eta_2 &= -\pi/4, \\ \tau &= -\theta/4 - \pi/4. \end{aligned} \quad (\text{A.10})$$

### 4. Waveplate angles for identity operator

Setting  $\varphi = \zeta = \xi = 0$ , Eq. A.1 becomes:

$$U(0, 0, 0) = \tilde{R}_y(0)\tilde{R}_z(0)\tilde{R}_y(0) = I, \quad (\text{A.11})$$

where waveplate angles are given by

$$\begin{aligned} \eta_1 &= -\pi/4, \\ \eta_2 &= -\pi/4, \\ \tau &= -\pi/4. \end{aligned} \quad (\text{A.12})$$

The angles in Passos et al. [74] are for the fast axis, measured from the horizontal and positive in the anticlockwise direction, when the beam passes the label-side first. To convert to an angle  $\theta$  of the fast axis measured from the vertical, positive in the clockwise direction for a beam entering the label-side first, we use  $\tau_{\text{lab}} = \pi/2 - \tau_{\text{Passos}}$ .

## Appendix B: Fringe visibility

The normalized photon counts as a function of motor steps in Fig. B.1 are fitted to the function  $f(\varphi) = a \cos(b\varphi + c) + d$ , where the parameters of the fit are  $a, b, c$  and  $d$ . We find the following values for the fit parameters:  $a = -0.445$ ,  $b = 0.235$ ,  $c = 0.0662$  and  $d = 0.531$  to reproduce Fig. 2 in the main text.

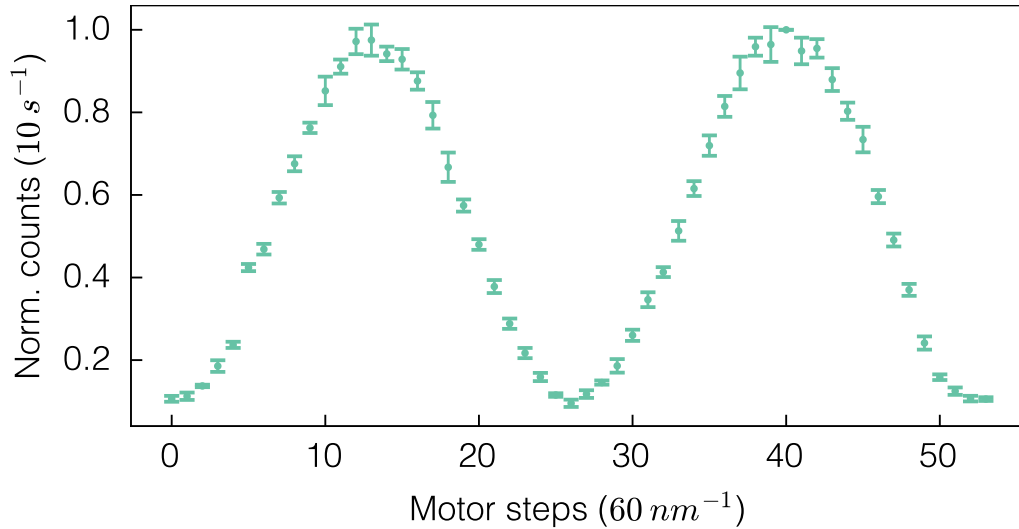


FIG. B.1: Normalized photon counts as a function of the phase difference between the two paths, varied by translating the mirror on a stage in steps of 60 nm (forward). Each data point is the average of 10 measurements. The error bars represent the standard deviation of the mean. The measurement setting was  $|A_1\rangle \langle A_1| \otimes |H_2\rangle \langle H_2|$ . The jump around the 6th step was due to joggling twice (120 nm step).

### Appendix C: Polarization measurement bases

We follow the conventions in Ref. [77] but deviate slightly as they consider a linear polarizer transmits vertically polarized light, while we consider a polarizing-beam-splitter that transmits horizontally polarized light. Moreover, our waveplate angles are always clockwise with respect to the vertical axis and fast axis of the waveplates. The 16 projective measurements we use in our tomography experiments and their waveplate angles are shown in Tab. C.1. Moreover, we use a Monte Carlo simulation with Poisson noise as the main source of noise [77] where we generate 100 density matrices, and derive from these the average and standard deviation of the quantities of interest.

$\hat{P}_1 \otimes \hat{P}_2$	$h_1$	$q_1$	$h_2$	$q_2$
$ V\rangle\langle V  \otimes  V\rangle\langle V $	$45^\circ$	$0^\circ$	$45^\circ$	$0^\circ$
$ V\rangle\langle V  \otimes  H\rangle\langle H $	$45^\circ$	$0^\circ$	$0^\circ$	$0^\circ$
$ H\rangle\langle H  \otimes  H\rangle\langle H $	$0^\circ$	$0^\circ$	$0^\circ$	$0^\circ$
$ H\rangle\langle H  \otimes  V\rangle\langle V $	$0^\circ$	$0^\circ$	$45^\circ$	$0^\circ$
$ L\rangle\langle L  \otimes  V\rangle\langle V $	$-22.5^\circ$	$0^\circ$	$45^\circ$	$0^\circ$
$ L\rangle\langle L  \otimes  H\rangle\langle H $	$-22.5^\circ$	$0^\circ$	$0^\circ$	$0^\circ$
$ D\rangle\langle D  \otimes  H\rangle\langle H $	$-22.5^\circ$	$45^\circ$	$0^\circ$	$0^\circ$
$ D\rangle\langle D  \otimes  V\rangle\langle V $	$-22.5^\circ$	$45^\circ$	$45^\circ$	$0^\circ$
$ D\rangle\langle D  \otimes  L\rangle\langle L $	$-22.5^\circ$	$45^\circ$	$-22.5^\circ$	$0^\circ$
$ D\rangle\langle D  \otimes  D\rangle\langle D $	$-22.5^\circ$	$45^\circ$	$-22.5^\circ$	$45^\circ$
$ L\rangle\langle L  \otimes  D\rangle\langle D $	$-22.5^\circ$	$0^\circ$	$-22.5^\circ$	$45^\circ$
$ V\rangle\langle V  \otimes  D\rangle\langle D $	$45^\circ$	$0^\circ$	$45^\circ$	$45^\circ$
$ H\rangle\langle H  \otimes  D\rangle\langle D $	$0^\circ$	$0^\circ$	$-22.5^\circ$	$45^\circ$
$ H\rangle\langle H  \otimes  R\rangle\langle R $	$0^\circ$	$0^\circ$	$22.5^\circ$	$0^\circ$
$ V\rangle\langle V  \otimes  R\rangle\langle R $	$45^\circ$	$0^\circ$	$22.5^\circ$	$0^\circ$
$ L\rangle\langle L  \otimes  R\rangle\langle R $	$-22.5^\circ$	$0^\circ$	$22.5^\circ$	$0^\circ$

TABLE C.1: Measurement settings for the tomography analysis of the two-photon polarization state. Coincidence counts are collected over a 10 second collection window. Here,  $|D\rangle = (|H\rangle + |V\rangle)/\sqrt{2}$ ,  $|A\rangle = (|H\rangle - |V\rangle)/\sqrt{2}$ ,  $|L\rangle = (|H\rangle + i|V\rangle)/\sqrt{2}$  and  $|R\rangle = (|H\rangle - i|V\rangle)/\sqrt{2}$ . The angles  $h$  and  $q$  denote angles for the HWPs and QWPs, respectively.

### Appendix D: Closed-form expression for the quantum Fisher information

For a pure state  $\rho$  and a generating Hamiltonian operator  $\hat{H}$ , the quantum Fisher information can be written in terms of the single-shot variance of  $\hat{H}$  [83] as

$$F_{\mathcal{Q}}(\rho, \hat{H}) = 4(\Delta H)^2, \quad (\text{D.1})$$

where  $(\Delta H)^2 = \langle \hat{H}^2 \rangle - \langle \hat{H} \rangle^2$ . In our particular case,  $\hat{H}$  is given by

$$\hat{H} = \frac{1}{2}(\hat{X}_1 \otimes \mathbb{1}_2 + \mathbb{1}_1 \otimes \hat{Z}_2). \quad (\text{D.2})$$

The expectation value of the above Hamiltonian operator with respect to the weighted graph state  $|\Gamma_{\phi_{12}}\rangle = [1 \ 1 \ 1 \ e^{i\phi_{12}}]^T/2$  can be written as

$$\langle \hat{H} \rangle = \langle \frac{1}{2}(\hat{X}_1 \otimes \mathbb{1}_2 + \mathbb{1}_1 \otimes \hat{Z}_2) \rangle = \frac{1}{2}(\langle \hat{X}_1 \otimes \mathbb{1}_2 \rangle + \langle \mathbb{1}_1 \otimes \hat{Z}_2 \rangle). \quad (\text{D.3})$$

The first expectation value becomes:

$$\begin{aligned} \langle \hat{X}_1 \otimes \mathbb{1}_2 \rangle &= \langle \Gamma_{\phi_{12}} | \hat{X}_1 \otimes \mathbb{1}_2 | \Gamma_{\phi_{12}} \rangle, \\ &= \frac{1}{4}(\langle 00 | + \langle 01 | + \langle 10 | + e^{-i\phi_{12}} \langle 11 | \rangle \cdot (|10\rangle + |11\rangle + |00\rangle + e^{i\phi_{12}} |01\rangle), \\ &= \frac{1}{4}(\langle 00|00\rangle + e^{i\phi_{12}} \langle 01|01\rangle + \langle 10|10\rangle + e^{-i\phi_{12}} \langle 11|11\rangle), \\ &= \frac{1}{4}(1 + e^{i\phi_{12}} + 1 + e^{-i\phi_{12}}) = \frac{1}{4}(2 + 2 \cos \phi_{12}) = \frac{1}{2}(1 + \cos \phi_{12}). \end{aligned} \quad (\text{D.4})$$

The second expectation value in Eq. D.3 becomes,

$$\begin{aligned}
\langle \mathbb{1}_1 \otimes \hat{Z}_2 \rangle &= \langle \Gamma_{\phi_{12}} | \mathbb{1}_1 \otimes \hat{Z}_2 | \Gamma_{\phi_{12}} \rangle, \\
&= \frac{1}{4} (\langle 00 | + \langle 01 | + \langle 10 | + e^{-i\phi_{12}} \langle 11 |) \cdot (|00\rangle - |01\rangle + |10\rangle - e^{i\phi_{12}} |11\rangle), \\
&= \frac{1}{4} (\langle 00|00\rangle - \langle 01|01\rangle + \langle 10|10\rangle - e^{i\phi_{12}} e^{-i\phi_{12}} \langle 11|11\rangle), \\
&= \frac{1}{4} (1 - 1 + 1 - 1) = 0.
\end{aligned} \tag{D.5}$$

Putting everything together, Eq. D.3 becomes,

$$\langle \hat{H} \rangle = \frac{1}{2} \left( \frac{1}{2} (1 + \cos \phi_{12}) + 0 \right) = \frac{1}{4} (1 + \cos \phi_{12}). \tag{D.6}$$

To calculate  $\langle \hat{H}^2 \rangle$ , we first write  $\hat{H}^2$ ,

$$\hat{H}^2 = \left[ \frac{1}{2} (\hat{X}_1 \otimes \mathbb{1}_2 + \mathbb{1}_1 \otimes \hat{Z}_2) \right]^2 = \frac{1}{4} (\hat{X}_1^2 \otimes \mathbb{1}_2 + \mathbb{1}_1 \otimes \hat{Z}_2^2 + 2\hat{X}_1 \otimes \hat{Z}_2). \tag{D.7}$$

Since  $\hat{X}^2 = \hat{Z}^2 = \mathbb{1}$ ,

$$\hat{H}^2 = \frac{1}{4} (2\mathbb{1}_1 \otimes \mathbb{1}_2 + 2\hat{X}_1 \otimes \hat{Z}_2) = \frac{1}{2} (\mathbb{1}_1 \otimes \mathbb{1}_2 + \hat{X}_1 \otimes \hat{Z}_2). \tag{D.8}$$

The expectation value is:

$$\langle \hat{H}^2 \rangle = \frac{1}{2} (\langle \mathbb{1}_1 \otimes \mathbb{1}_2 \rangle + \langle \hat{X}_1 \otimes \hat{Z}_2 \rangle) = \frac{1}{2} (1 + \langle \hat{X}_1 \otimes \hat{Z}_2 \rangle). \tag{D.9}$$

The second expectation value in the expression evaluates to

$$\begin{aligned}
\langle \hat{X}_1 \otimes \hat{Z}_2 \rangle &= \langle \Gamma_{\phi_{12}} | \hat{X}_1 \otimes \hat{Z}_2 | \Gamma_{\phi_{12}} \rangle, \\
&= \frac{1}{4} (\langle 00 | + \langle 01 | + \langle 10 | + e^{-i\phi_{12}} \langle 11 |) \cdot (|10\rangle - |11\rangle + |00\rangle - e^{i\phi_{12}} |01\rangle), \\
&= \frac{1}{4} (\langle 00|00\rangle + -e^{i\phi_{12}} \langle 01|01\rangle + \langle 10|10\rangle - e^{-i\phi_{12}} \langle 11|11\rangle), \\
&= \frac{1}{4} (1 - e^{i\phi_{12}} + 1 - e^{-i\phi_{12}}) = \frac{1}{4} (2 - 2 \cos \phi_{12}) = \frac{1}{2} (1 - \cos \phi_{12}).
\end{aligned} \tag{D.10}$$

Collecting everything, Eq. D.9 becomes

$$\langle \hat{H}^2 \rangle = \frac{1}{2} \left( 1 + \frac{1}{2} (1 - \cos \phi_{12}) \right) = \frac{1}{4} (3 - \cos \phi_{12}). \tag{D.11}$$

The single-shot variance for  $\hat{H}$  is then given by

$$\begin{aligned}
(\Delta \hat{H})^2 &= \langle \hat{H}^2 \rangle - \langle \hat{H} \rangle^2, \\
&= \frac{1}{4} (3 - \cos \phi_{12}) - \left[ \frac{1}{4} (1 + \cos \phi_{12}) \right]^2, \\
&= \frac{4(3 - \cos \phi_{12})}{16} - \frac{1 + 2 \cos \phi_{12} + \cos^2 \phi_{12}}{16}, \\
&= \frac{12 - 4 \cos \phi_{12} - 1 - 2 \cos \phi_{12} - \cos^2 \phi_{12}}{16}, \\
&= \frac{11 - 6 \cos \phi_{12} - \cos^2 \phi_{12}}{16}.
\end{aligned} \tag{D.12}$$

To get the expression for the QFI, we multiply the expression above by 4

$$F_{\mathcal{Q}}(|\Gamma_{\phi_{12}}\rangle \langle \Gamma_{\phi_{12}}|, \hat{H}) = \frac{11 - 6 \cos \phi_{12} - \cos^2 \phi_{12}}{4}, \tag{D.13}$$

the QFI is independent of the sensing phase  $\theta$  and depends only on the graph weight  $\phi_{12}$ . When  $\phi_{12} = \pi$ , we have  $F_{\mathcal{Q}} = 4$ , which is the HL for  $N = 2$ , on the other hand, when  $\phi_{12} = 0$  we have  $F_{\mathcal{Q}} = 1$ , which is below the SQL for  $N = 2$  ( $F_{\mathcal{Q}} = 2$ ). Therefore, a range of enhancements in the precision  $(\Delta\theta)^2$  is expected depending on the weight  $\phi_{12}$ , according to the QCRB.

### Appendix E: Local Pauli measurements

We perform an exhaustive numerical search over all  $4^2 = 16$  possible local Pauli product operators at each graph weight  $\phi_{12}$  of interest to find the operator  $\hat{A} = \hat{A}_1 \otimes \hat{A}_2$  that yields the smallest value for the estimator variance  $(\Delta\theta)^2$ . Tab. E.1 shows the optimal local Pauli operators for various graph weights  $\phi_{12}$ , when  $\theta = 0$ . Here, when multiple operators have same value for  $(\Delta\theta)^2$  we choose one with the largest derivative magnitude. Near the operating point  $\theta = 0$ , the derivative and variance of the operators  $\hat{A}$  are robust enough to changes in  $\theta$ . Particularly, the derivative reaches a maxima around  $\theta = 0$  and  $\langle \hat{A} \rangle$  has an inflection point around  $\theta = 0$ . This is justification for approximating the derivative here via finite differences. Fig. E.1 shows the expectation value of  $\langle \hat{A} \rangle$ , its square  $\langle \hat{A}^2 \rangle$ , derivative  $\partial_\theta \langle \hat{A} \rangle$  and variance  $(\Delta A)^2$  of the optimal local Pauli operators as a function of the encoded phase  $\theta \in [0, 2\pi)$  for different graph weights.

$\phi_{12}$	$\hat{A}$	$\langle \hat{A} \rangle$	$ \partial_\theta \langle \hat{A} \rangle $	$(\Delta\theta)^2$
$\pi$	$\hat{Z}_1 \otimes \hat{Y}_2$	0.00	2.00	0.25
$7\pi/8$	$\hat{Z}_1 \otimes \hat{Y}_2$	-0.19	1.92	0.26
$3\pi/4$	$\hat{Z}_1 \otimes \hat{Y}_2$	-0.35	1.71	0.30
$5\pi/8$	$\hat{Z}_1 \otimes \hat{Y}_2$	-0.46	1.38	0.41
$\pi/2$	$\hat{Z}_1 \otimes \hat{Y}_2$	-0.50	1.0	0.75
$3\pi/8$	$\hat{Y}_1 \otimes \hat{Y}_2$	0.31	0.92	1.06
$\pi/4$	$\mathbb{1}_1 \otimes \hat{Y}_2$	0.35	0.85	1.20
$\pi/8$	$\mathbb{1}_1 \otimes \hat{Y}_2$	0.19	0.96	1.04
0	$\mathbb{1}_1 \otimes \hat{Y}_2$	0.00	1.00	1.00

TABLE E.1: Expectation values and  $(\Delta\theta)^2$  obtained with optimal local Pauli measurements for varied weightings  $\phi_{12}$ .

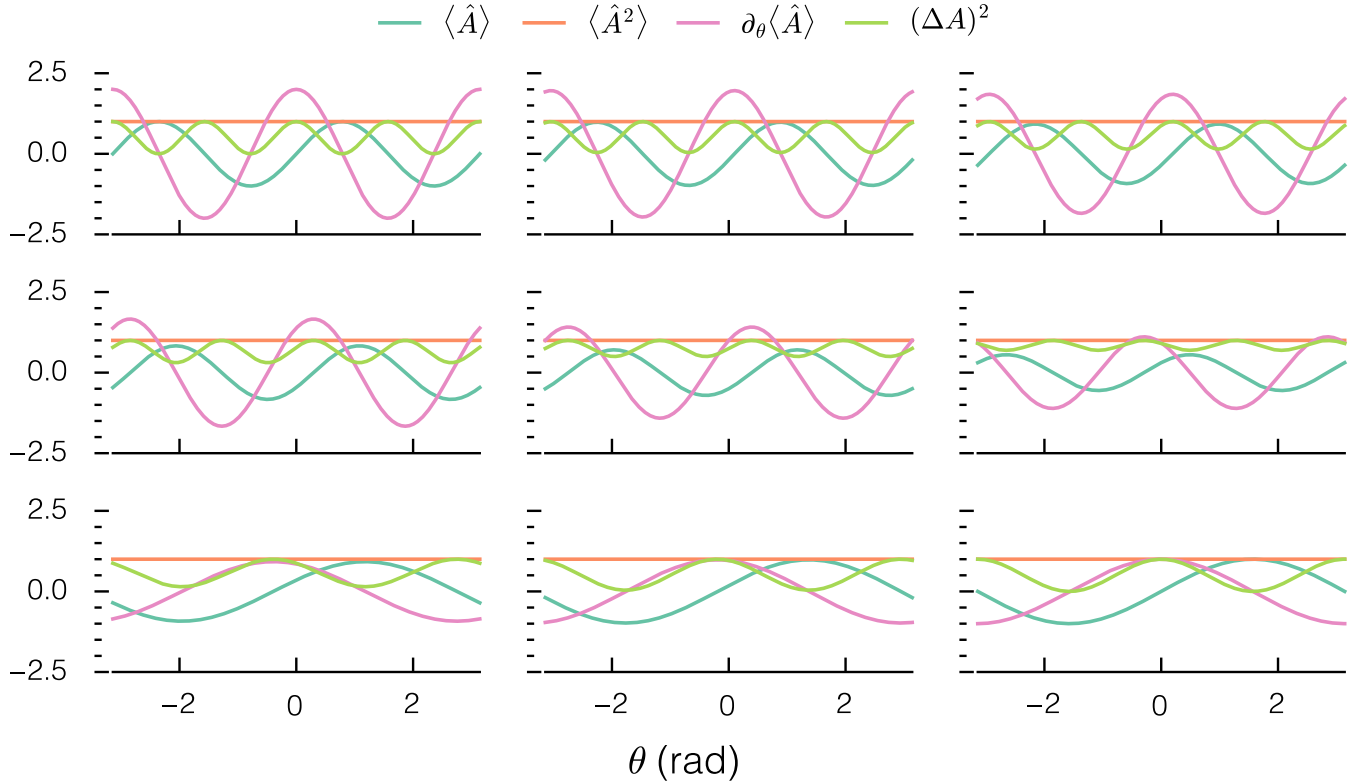


FIG. E.1: Top left to bottom right: The expectation value of  $\langle \hat{A} \rangle$  (blue line), its square  $\langle \hat{A}^2 \rangle$  (orange line), derivative  $\partial_\theta \langle \hat{A} \rangle$  (green line) and variance  $(\Delta A)^2$  (red line) as a function of the encoded phase  $\theta \in [0, 2\pi)$  for graph weights  $\phi_{12} \in \{\pi, \frac{7\pi}{8}, \frac{3\pi}{4}, \frac{5\pi}{8}, \frac{\pi}{2}, \frac{3\pi}{8}, \frac{\pi}{4}, \frac{\pi}{8}, 0\}$ . Here,  $\hat{A} = \hat{A}_1 \otimes \hat{A}_2$  is the optimal local Pauli operator at the phase encoding  $\theta = 0$ . These operators can be found in Tab. E.1.

## Appendix F: Bootstrapping

For a particular observable  $\hat{A}$ , we measure four combinations of polarization projectors, labeled  $k \in \{++, +-, -+, --\}$ , with corresponding weights  $w_k \in \{\pm 1\}$  fixed by the chosen basis. For example, the observable  $\hat{A} = \hat{Z}_1 \otimes \hat{Z}_2$  has the weights  $w_{++} = w_{--} = +1$ ,  $w_{+-} = w_{-+} = -1$ , while  $\hat{A} = \mathbb{1}_1 \otimes \hat{Y}_2$  has the weights  $w_{++} = w_{-+} = +1$  and  $w_{+-} = w_{--} = -1$ . Let  $N_k$  be the observed coincidences in one acquisition and  $N = \sum_k N_k$  the total coincidences for that setting. The estimator of the expectation value  $\langle \hat{A} \rangle$  is

$$\hat{E} = \frac{\sum_k w_k N_k}{\sum_k N_k} = \frac{1}{N} \sum_k w_k N_k. \quad (\text{F.1})$$

Our data are naturally grouped into acquisition bins (runs) indexed by  $\ell = 1, \dots, L$ , where  $L = 6$ . Each bin contains the four photon counts  $N_{k,\ell}$  collected over a 10-second interval. One bootstrap replicate proceeds as follows (and is performed independently for every setting used below):

1. Draw, with replacement,  $L$  bin indices  $\ell_1, \dots, \ell_L \in \{1, \dots, L\}$ .
2. Form resampled totals  $N_k^* = \sum_{j=1}^L N_{k,\ell_j}$  and  $\nu^* = \sum_k N_k^*$ .
3. Set  $\hat{E}^* = [\sum_k w_k N_k^*] / \nu^*$ .

Repeating for  $b = 1, \dots, \mu$  gives the set  $\{\hat{E}_b^*\}_{b=1}^\mu$  and  $\{1 - (\hat{E}_b^*)^2\}_{b=1}^\mu$ . We report point estimates as means of the bootstrap samples and 95% confidence intervals via the empirical 2.5th and 97.5th percentiles.

### 1. Poisson noise

Note that we are interested in the single-shot variance  $(\Delta A)^2$ , where the noise for a single pair of entangled photons in the state  $|\Gamma_{\phi_{12}}\rangle$  originates from quantum fluctuations only. However, in our experiment we are measuring coincidence counts corresponding to many pairs of entangled photons over a fixed period of 10 seconds, where the number of shots (photon pairs) fluctuates due to Poisson noise from the SPDC process. This is equivalent to having a sample size  $\nu$  that varies. Let  $\nu^*$  be the varying sample size due to Poisson noise, i.e.,  $\nu^* = \nu + \delta\nu$ , where  $\nu$  is some fixed number of shots and  $\delta\nu \sim \mathcal{N}(0, \sigma_\nu^2)$  is a Gaussian noise term with mean of zero and variance  $\sigma_\nu^2$ . The expectation value of the variance of the estimator  $\hat{E}$ , i.e.,  $(\Delta \hat{E})^2$ , is then given by:

$$E[(\Delta \hat{E})^2] = E\left[\frac{(\Delta A)^2}{\nu^*}\right]. \quad (\text{F.2})$$

Taking  $(\Delta A)^2$  and  $\nu^*$  to be independent, we have:

$$E\left[\frac{(\Delta A)^2}{\nu^*}\right] = E\left[\frac{1}{\nu^*}\right] E[(\Delta A)^2]. \quad (\text{F.3})$$

The first term on the right hand side is:

$$E\left[\frac{1}{\nu^*}\right] = E\left[\frac{1}{\nu + \delta\nu/\nu}\right] \simeq E\left[\frac{1}{\nu}\right] = \frac{1}{\nu}, \quad (\text{F.4})$$

where the final approximation is due to  $\delta\nu \approx \sqrt{\nu}$  for Poisson noise and  $\delta\nu/\nu = 1/\sqrt{\nu} \ll 1$  for large  $\nu$ . Therefore we have:

$$E[(\Delta A)^2] = \nu E[(\Delta \hat{E})^2]. \quad (\text{F.5})$$

The above relation shows that for large  $\nu$ , the measured variance from the bootstrap procedure,  $E[(\Delta \hat{E})^2]$ , coming from  $\mu$  samples, i.e.,

$$E[(\Delta \hat{E})^2] = \frac{1}{\mu} \sum_{b=1}^\mu \left(1 - (\hat{E}_b^*)^2\right), \quad (\text{F.6})$$

can be used to obtain the single-shot variance  $E[(\Delta A)^2]$ , using the average count  $\nu = \frac{1}{\mu} \sum_{b=1}^\mu \nu_b^*$ . The same approach can be followed for other expectation values, such as  $E[\hat{E}]$ .

## 2. Bootstrap for the 2-point finite-difference derivative

The 2-point finite-difference derivative at  $\theta^*$  with a fixed shift  $h > 0$  ( $h = 5^\circ$  in our analysis) is estimated from measurements at  $\theta^* \pm h$  as

$$\left. \partial_\theta \widehat{\langle \hat{A} \rangle} \right|_{\theta=\theta^*} \approx \frac{\widehat{E}(\theta^* + h) - \widehat{E}(\theta^* - h)}{2h}. \quad (\text{F.7})$$

At each setting  $s \in \{\theta^* - h, \theta^* + h\}$ , we perform the bin bootstrap above to obtain  $\{\widehat{E}_b^*(s)\}_{b=1}^\mu$ . For each replicate  $b$ , define

$$\partial_\theta \widehat{\langle \hat{A} \rangle}_b^* = \frac{\widehat{E}_b^*(\theta^* + h) - \widehat{E}_b^*(\theta^* - h)}{2h}. \quad (\text{F.8})$$

The point estimate and the 95% CI are the mean and the percentile interval of  $\{\partial_\theta \widehat{\langle \hat{A} \rangle}_b^*\}_{b=1}^\mu$ .

## 3. Bootstrap for the estimator variance

Consider the ratio for the estimator variance

$$\widehat{\mathcal{R}}(\theta) = \frac{1 - \widehat{E}(\theta)^2}{|\partial_\theta \widehat{\langle \hat{A} \rangle}|}. \quad (\text{F.9})$$

To obtain the uncertainty for  $\widehat{\mathcal{R}}(\theta)$ , we use the same bin bootstrap method independently at  $\theta^*$ ,  $\theta^* - h$  and  $\theta^* + h$ . For each bootstrap replicate  $b$ ,

$$\widehat{\mathcal{R}}_b^*(\theta) = \frac{1 - (\widehat{E}_b^*(\theta^*))^2}{|\partial_\theta \widehat{\langle \hat{A} \rangle}_b^*|^2}, \quad (\text{F.10})$$

with a small, fixed threshold applied to the denominator to avoid numerical artefacts when the derivative is very small:

$$|\partial_\theta \widehat{\langle \hat{A} \rangle}_b^*|^2 \leftarrow \max(|\partial_\theta \widehat{\langle \hat{A} \rangle}_b^*|^2, \varepsilon), \quad (\text{F.11})$$

with  $\varepsilon$  fixed *a priori* (we used  $\varepsilon \sim 10^{-12}$ ). We report the mean of  $\{\widehat{\mathcal{R}}_b^*(\theta)\}_{b=1}^\mu$  as the point estimate and the 95% percentile interval as its confidence interval.

## Appendix G: Local general-axis measurements

The central task is to find the optimal two-qubit observable,  $\hat{A}$ , that minimizes the estimator variance, where  $\hat{A}$  is a product of two local single-qubit observables. Each local observable ( $\hat{A}_1$  and  $\hat{A}_2$ ) is defined by its corresponding axis on the Bloch sphere using two angles: the polar angle  $\beta$  and the azimuthal angle  $\alpha$ . The optimization routine finds the four optimal parameters:  $(\beta_1, \alpha_1, \beta_2, \alpha_2)$ . The search is performed using a global optimization technique called Differential Evolution, which explores the four-dimensional parameter space. This is often followed by a local refinement step using Powell's method to fine-tune the minimum. Both algorithms are available in the Python library SciPy. We also add a small soft penalty term proportional to  $1/|\partial_\theta \widehat{\langle \hat{A} \rangle}|$  to the objective function. This ensures the optimizer favors solutions that not only yield low variance but also maintain a high, measurable signal for the derivative. Moreover, after optimization, the routine samples a small neighborhood around the best solution and re-ranks these near-optimal points. This is done by first selecting all points whose variance is within a small tolerance of the minimum, and from that subset, we choose the point with the largest derivative  $|\partial_\theta \widehat{\langle \hat{A} \rangle}|$ . To physically realize the optimal local general-axis measurements, we need to realize the projectors for these corresponding operators using a QWP, HWP, and PBS that only transmits horizontally polarized photons. To find the waveplate angles corresponding to each projector, we numerically minimize the objective function  $F_\pm(h, q)$

$$F_\pm(h^{(\pm)}, q^{(\pm)}) = 1 - \langle H | \text{HWP}(h^{(\pm)}) \text{QWP}(q^{(\pm)}) | \beta, \alpha, \pm \rangle. \quad (\text{G.1})$$

Here,  $F_\pm(h, q)$  will reach a minimum when  $\langle H | \text{HWP}(h^{(\pm)}) \text{QWP}(q^{(\pm)}) = \langle \pm, \alpha, \beta |$ , *i.e.*, acting with  $\text{HWP}(h^{(\pm)}) \text{QWP}(q^{(\pm)})$  on  $|\beta, \alpha, \pm \rangle$  maps it to  $|H \rangle$  (transmission port of the polarizing beam splitter). The results of the optimization routines are shown in Tab. G.1, which shows the waveplate angles for each projector, *i.e.*,  $++$ ,  $+-$ ,  $-+$ ,  $--$  and the corresponding polar and azimuthal angles.

$\phi_{12}$	$\beta_1$	$\alpha_1$	$h_1^{(+)}$	$q_1^{(+)}$	$h_1^{(-)}$	$q_1^{(-)}$	$\beta_2$	$\alpha_2$	$h_2^{(+)}$	$q_2^{(+)}$	$h_2^{(-)}$	$q_2^{(-)}$	$\langle \hat{A} \rangle$	$ \partial_\theta \langle \hat{A} \rangle $	$(\Delta\theta)^2$
$\pi$	44.64	-89.76	-78.89	-0.12	-56.23	89.88	90.00	44.60	-11.37	45.00	-56.37	45.00	0.01	2.00	0.25
$7\pi/8$	52.96	-95.72	-74.97	3.76	-56.27	-86.24	85.73	-140.95	-78.61	-47.75	75.86	42.25	0.24	1.92	0.26
$3\pi/4$	60.44	-102.31	-70.30	10.30	-54.40	-79.70	81.59	-147.18	-78.10	-49.99	73.11	40.01	0.46	1.69	0.28
$5\pi/8$	64.54	-110.61	84.70	-71.76	68.54	18.24	79.36	-159.05	24.80	39.31	69.80	39.31	0.53	1.50	0.32
$\pi/2$	68.27	-120.53	89.68	-64.06	71.36	25.99	79.26	-174.10	21.25	39.60	63.35	-50.40	0.55	1.34	0.39
$3\pi/8$	73.05	-131.87	-84.99	-57.27	72.72	32.72	81.22	168.72	17.47	40.52	68.05	-49.48	0.55	1.17	0.51
$\pi/4$	90.00	39.58	-12.61	45.00	-57.61	45.00	90.00	112.50	84.38	-45.00	-84.38	45.00	0.49	1.05	0.69
$\pi/8$	90.00	-158.36	27.91	45.00	62.09	-45.00	90.00	-78.75	87.19	-45.00	-87.19	45.00	0.00	1.05	0.90
0	90.00	180.00	-22.50	45.00	-67.50	-45.00	90.00	90.00	-90.00	-45.00	-90.00	45.00	0.00	1.00	1.00

TABLE G.1: Optimal local general-axis measurement parameters ( $\beta_i, \alpha_i$ ) and implementing waveplate settings ( $h_i, q_i$ ) for varied graph weights  $\phi_{12}$ . Waveplate columns correspond to the QWP/HWP angles for the (+) or (-) projector of each qubit. Also shown are the resulting minimum estimator variance  $(\Delta\theta)^2$ , expectation values  $\langle \hat{A} \rangle$ , and derivatives  $|\partial_\theta \langle \hat{A} \rangle|$ . Angles are reported in degrees.

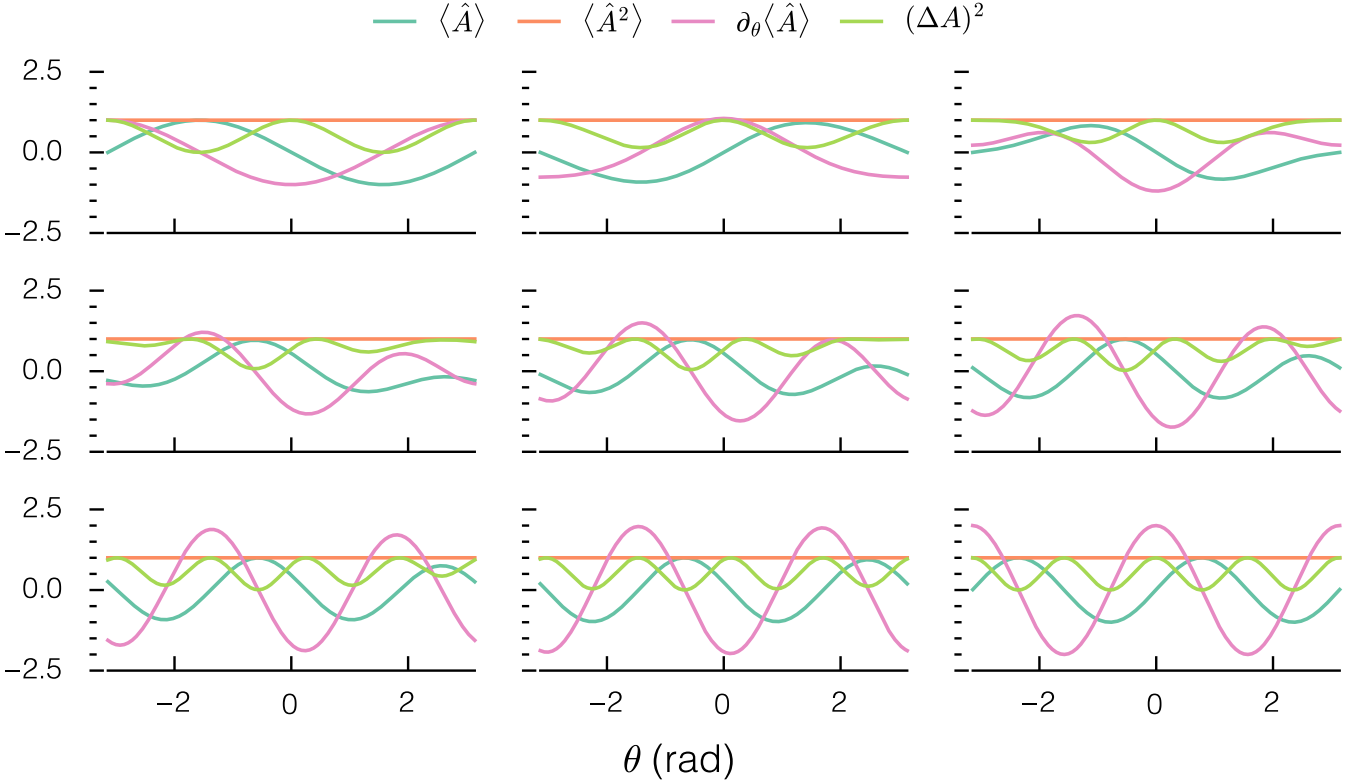


FIG. G.1: Top left to bottom right: The expectation value of  $\langle \hat{A} \rangle$  (blue line), its square  $\langle \hat{A}^2 \rangle$  (orange line), derivative  $\partial_\theta \langle \hat{A} \rangle$  (green line) and variance  $(\Delta A)^2$  (red line) as a function of the encoded phase  $\theta \in [0, 2\pi)$  for graph weight  $\phi_{12} \in \{\pi, \frac{7\pi}{8}, \frac{3\pi}{4}, \frac{5\pi}{8}, \frac{\pi}{2}, \frac{3\pi}{8}, \frac{\pi}{4}, \frac{\pi}{8}, 0\}$ . Here,  $\hat{A} = \hat{A}_1 \otimes \hat{A}_2$  is the optimal general-axis operator at the phase encoding  $\theta = 0$ . These operators can be found in Tab. G.1.

Similar to the local Pauli observables, near the operating point  $\theta = 0$ , the derivative and variance of the local general-axis operators  $\hat{A}$  are robust to changes in  $\theta$ . Fig. G.1 shows the expectation value of  $\langle \hat{A} \rangle$ , its square  $\langle \hat{A}^2 \rangle$ , derivative  $\partial_\theta \langle \hat{A} \rangle$  and variance  $(\Delta A)^2$  of the optimal local general-axis operators as a function of the encoded phase  $\theta \in [0, 2\pi)$  for different graph weights.